

# Lack of evidence for increased transcriptional noise in aged tissues

Olga Ibáñez-Solé<sup>1,5†</sup>, Alex M. Ascensión<sup>1,5†</sup>, Marcos J. Araúzo-Bravo<sup>1,2,3,4\*</sup>, Ander Izeta<sup>5,6\*</sup>

\*For correspondence:

ander.izeta@biodonostia.org (AI);  
mararabra@yahoo.co.uk (MJA-B)

<sup>†</sup>These authors contributed equally to this work

<sup>1</sup>Biodonostia Health Research Institute, Computational Biology and Systems Biomedicine Group, Donostia-San Sebastián, Spain; <sup>2</sup>Biodonostia Health Research Institute, Computational Biomedicine Data Analysis Platform, Donostia-San Sebastián, Spain; <sup>3</sup>CIBER of Frailty and Healthy Aging (CIBERfes), Madrid, Spain; <sup>4</sup>IKERBASQUE, Basque Foundation for Science, Bilbao, Spain; <sup>5</sup>Biodonostia Health Research Institute, Tissue Engineering group, Donostia-San Sebastián, Spain; <sup>6</sup>Tecnun-University of Navarra, Donostia-San Sebastián, Spain.

**Abstract** Aging is often associated with a loss of cell type identity that results in an increase in transcriptional noise in aged tissues. If this phenomenon reflects a fundamental property of aging remains an open question. Transcriptional changes at the cellular level are best detected by single-cell RNA sequencing (scRNASeq). However, the diverse computational methods used for the quantification of age-related loss of cellular identity have prevented reaching meaningful conclusions by direct comparison of existing scRNASeq datasets. To address these issues we created *Decibel*, a Python toolkit that implements side-to-side four commonly used methods for the quantification of age-related transcriptional noise in scRNASeq data. Additionally, we developed *Scallop*, a novel computational method for the quantification of membership of single cells to their assigned cell type cluster. Cells with a greater *Scallop* membership score are transcriptionally more stable. Application of these computational tools to seven aging datasets showed large variability between tissues and datasets, suggesting that increased transcriptional noise is not a universal hallmark of aging. To understand the source of apparent loss of cell type identity associated with aging, we analyzed cell type-specific changes in transcriptional noise and the changes in cell type composition of the mammalian lung. No robust pattern of cell type-specific transcriptional noise alteration was found across aging lung datasets. In contrast, age-associated changes in cell type composition of the lung were consistently found, particularly of immune cells. These results suggest that claims of increased transcriptional noise of aged tissues should be reformulated.

## Introduction

Concomitant to the large repertoire of known age-associated changes at the cellular level, an increase in transcriptional variability is generally assumed to characterize aged cells and tissues (*Nikopoulou et al., 2019; Uyar et al., 2020; Mendenhall et al., 2021; Vijg, 2021*). This phenomenon was first described by Vijg and colleagues as an *age-related increase in transcriptional noise* (*Bahar et al., 2006*), which is still the most commonly used term (*Warren et al., 2007; Enge et al., 2017; Angelidis et al., 2019*). *Transcriptional noise* is here defined as the measured level of variation in gene expression among cells supposed to be identical (*Raser and O'Shea, 2005*). Later, similar findings have been reported as an increase in *identity noise* (*Salzer et al., 2018*), *cell-cell heterogeneity* (*Kimmel et al., 2019*), *cell-to-cell variability* (*Martinez-Jimenez et al., 2019; Ximerakis et al., 2019*), or

42 *loss of cellular identity* in aged tissues (**Solé-Boldo et al., 2020; Izgi et al., 2022**). While all these claims  
43 have in common the notion of cells expressing their core transcriptional program or *transcriptomic*  
44 *signature* in a loose way, there are important methodological differences between the published  
45 reports that deserve further scrutiny.

46 Early studies were based on the quantification of the variance associated with the expression of  
47 a few pre-selected transcripts by real-time PCR, on bulk cell and tissue samples (**Bahar et al., 2006**;  
48 **Warren et al., 2007**). With the advent of single-cell RNA sequencing (scRNAseq) technologies, whole-  
49 transcriptome variability on aged tissues was studied at the single-cell level. A pioneering study on  
50 human pancreas by Quake and colleagues found an age-related increase in transcriptional noise  
51 specific to pancreatic  $\beta$  cells (**Enge et al., 2017**). The authors introduced a definition of transcriptional  
52 noise that was based on whole-transcriptome variability: the ratio between biological and technical  
53 variation, where the latter was inferred from External RNA Controls Consortium (ERCC) spike-in  
54 variability. As ERCC spike-in controls are not included in every scRNAseq experiment, they proposed  
55 two alternative methods that were based on the notion of "distance to centroid": the greater the  
56 gene-based distance between cells of the same cell type, the greater the transcriptional noise  
57 associated with them. One of them measured the Euclidean distance to the cell type mean per  
58 individual, using the whole transcriptome. The other one measured the Euclidean distance between  
59 each cell and the tissue mean, using a set of invariant genes. Soon after, loss of identity was reported  
60 in aged murine dermal fibroblasts by measuring the coefficient of variation of the distances between  
61 each highly variable gene between the two main fibroblast clusters (**Salzer et al., 2018**). Similar  
62 findings were published in early activated CD4+ T cells, based on the observation that the fraction  
63 of cells that expressed the core activation program was lower in old animals (**Martinez-Jimenez**  
64 **et al., 2019**). A study on murine aging lung found an increase in cellular heterogeneity in most  
65 (but not all) cell types (**Angelidis et al., 2019**), based on the distance-to-mean method of **Enge et al.**  
66 Later, a study on murine lung, spleen and kidney corroborated by Euclidean distance-to-centroid  
67 methods an age-related increase in cell-to-cell variability, albeit present in some cell types only  
68 (**Kimmel et al., 2019**). In contrast, a study in murine aging brain found no increase in transcriptional  
69 heterogeneity associated with aging (**Ximerakis et al., 2019**). Overall, these results suggest that the  
70 purported age-associated increase in transcriptional noise might be restricted to particular cell  
71 types or tissues.

72 Of note, alternative explanations to the variability in the expression of individual genes being  
73 the basis for increased transcriptional noise do exist. Among others, the lack of balance between  
74 spliced and unspliced mRNAs (**Gupta et al., 2021**) and the existence of dysregulated gene regulatory  
75 networks (**Mishra et al., 2021**) have been proposed. In fact, Bashan and colleagues developed a  
76 novel computational tool to measure age-related loss of gene-to-gene transcriptional coordination  
77 (what they called *Global Coordination Level* or GCL), and reported a GCL decrease in aging cells  
78 across diverse organisms and cell types, which was also associated with a high mutational load  
79 (**Levy et al., 2020**). In a nutshell, these authors suggested that the observations of age-associated  
80 increase in cell-to-cell variability were restricted to specific cell types and tissues, but not general-  
81 ized. Instead, they proposed that transcriptional dysregulation occurs at the level of gene-to-gene  
82 coordination. Despite the numerous attempts at measuring transcriptional noise in aged tissues,  
83 several challenges remain: (i) there are important differences in between studies with regard to the  
84 definition of *transcriptional noise* and the computational methods used to quantify it; (ii) studies  
85 focused mostly on single datasets of different tissues and cell types, while it is well known that both  
86 the inter-tissue and the inter-cellular variability might be significant; and (iii) little to no attention was  
87 given to the fact that cellular composition of aged organs shows relevant variability as compared to  
88 the young (**Nalapareddy et al., 2022**).

89 In the present work, we aimed to systematically measure age-associated transcriptional noise  
90 across different tissues and species, testing diverse computational methods in parallel. The main  
91 goals of the study were to substantiate claims of age-associated transcriptional noise increase  
92 and determine whether it presents a cell type-specific pattern. For this, we took advantage of

93 the large number of aging mouse and human scRNAseq datasets that are publicly available, and  
94 developed two computational tools (*Decibel* and *Scallop*) to analyze them by focusing on two aspects:  
95 age-related transcriptional noise and changes in cell type composition.

96 **Results**

97 ***Decibel: a Python toolkit for transcriptional noise quantification***

98 We developed a Python toolkit for the quantification of transcriptional noise in scRNAseq, where we  
99 implemented the four main families of methods that have been used in the literature to measure  
100 loss of cell type identity associated with aging (Figure 1A). The first method, which we refer to as  
101 *biological variation over technical variation*, takes the Pearson's correlation distance between each  
102 cell and the mean expression vector of its corresponding cell type for that individual, using the  
103 whole transcriptome in the calculation. It then divides this correlation by the ERCC-based distance  
104 between each cell and its cell type mean. This method can only be used when ERCC spike-ins  
105 have been included in the experimental design. The second method computes the gene-based  
106 Euclidean distance between each cell's expression vector and its cell type mean expression vector  
107 per donor/individual. The third one computes the Euclidean distance between each cell and the  
108 average gene expression across cell types, using a set of invariant genes. Invariant genes are  
109 selected by splitting the whole transcriptome into ten equally-sized bins according to their mean  
110 expression. Then, the two bins with the most extreme expression values are discarded and the  
111 10% with the highest coefficient of variation within each of the remaining bins are selected. The  
112 fourth one is the GCL. Its original formulation takes a dataset containing a single cell type and it  
113 randomly splits its transcriptome into two halves, then computes the dependency between them as  
114 the batch-corrected distance correlation ([Levy et al., 2020](#)). The GCL is obtained by averaging this  
115 dependency over  $k$  iterations. We implemented an extension of this method so that it could be used  
116 in datasets containing several cell types, by computing the GCL averaged over 50 iterations for each  
117 cell type of the same individual. Therefore, our implementation outputs a GCL score per cell type  
118 and individual rather than a transcriptional variability measure per cell. The Python implementation  
119 of these four methods is available at <https://gitlab.com/olgaibanez/decibel>.

120 ***Scallop membership score accurately identifies transcriptionally noisy cells***

121 In addition to implementing existing methods, we developed *Scallop*, a novel tool for the quantifi-  
122 cation of the degree of loss of cell type identity in scRNAseq data (Figure 1B). *Scallop* measures  
123 the membership of each cell to a particular cluster by iteratively running a clustering algorithm on  
124 randomly selected subsets of cells and computing the fraction of iterations a cell was assigned to a  
125 particular cluster. Thus, cluster membership takes values between 0 and 1. *Scallop* relies on the  
126 assumption that the more consistently a cell is assigned to a particular cluster across bootstrap  
127 iterations, the greater its transcriptional stability. Conversely, a cell being assigned to different  
128 clusters across iterations is indicative of a greater transcriptional variation. Therefore, we quantify  
129 loss of cell type identity as  $1 - \text{membership}$ .

130 In order to characterize and validate the performance of our method, we conducted three  
131 experiments. First, we compared the output of *Scallop* to the transcriptional noise measured using  
132 the methods implemented in *Decibel* on 8,278 human T cells drawn from the Peripheral Blood  
133 Mononuclear Cell (PBMC) 20K dataset from 10x Genomics. Clustering revealed three main T cell  
134 subtypes, which we annotated according to their expression of *CD4* and *CD8* markers (Figure 1 -  
135 Supplement 1A). Then, we measured transcriptional variability and gene coordination level using  
136 *Decibel* and inspected the distribution of variability scores over the Uniform Manifold Approximation  
137 and Projection (UMAP) plots (Figure 1 - Supplement 1B). Unlike distance-to-centroid methods, *Scallop*  
138 detected transcriptionally noisy cells that lie in between transcriptionally stable T cell subtypes on  
139 the UMAP plot. GCL yielded different coordination levels for each T cell subtype, but the method  
140 does not allow for comparisons between individual cells, as it outputs a single score per cell type.

141 In addition, we plotted the 10% most transcriptionally stable and unstable cells according to the  
142 *Euclidean distance to the cell type mean* and *Scallop* methods (Figure 1 - Supplement 1C). These  
143 analyses suggested that *Scallop*'s membership score outperforms distance-to-centroid methods at  
144 discriminating between noisy cells lying in between clusters and more transcriptionally robust cells  
145 constituting the core of T cell subtypes.

146 Next, we analyzed *Scallop*'s robustness in response to input parameters, namely, the number  
147 of bootstrap iterations and the fraction of cells used in each iteration. We ran *Scallop* on five  
148 independent scRNAseq datasets with different size and cluster composition (see Appendix 1),  
149 and studied the convergence of *Scallop* membership scores for a wide range of values (Figure  
150 1 - Supplement 2). The median correlation distance between membership scores decreased as  
151 we increased the number of bootstrap iterations (`n_trials`) and the fraction of cells used in  
152 each iteration (`frac_cells`). We concluded that *Scallop*'s output is robust to changes in its input  
153 parameter values, the results suggesting that `frac_cells > 0.8` and `n_trials > 30` are appropriate  
154 parameter values for most datasets (Figure 1 - Supplement 2).

155 Finally, we studied the relationship between *Scallop* membership score and robust gene marker  
156 expression, by comparing the statistical significance of the output of differential expression analysis  
157 between cell type clusters, conducted on stable and unstable cells. For this, we analyzed six cell  
158 types and subtypes (*CD4* and *CD8* T cells, *CD14* and *FCGR3A* monocytes, dendritic cells, and NK  
159 cells) from the [PBMC 3K dataset](#) from 10x Genomics. Cells with a higher *Scallop* membership to  
160 their cluster differentially expressed cell type-specific markers with greater statistical significance  
161 than low-membership cells (Figure 1 - Supplement 3). Overall, these results showed that *Scallop*  
162 membership is related to a more robust expression of gene markers defining cell types than other  
163 existing methods.

#### 164 **Increased transcriptional noise is not a universal hallmark of aging**

165 To determine if aging is associated with a generalized increase in transcriptional noise at the tissue  
166 level, we used *Scallop* to compare the average degree of membership of young and old cells to  
167 their cell type cluster in scRNAseq datasets of various tissues (Figure 2). For the initial analysis, we  
168 selected seven datasets where transcriptional noise had already been measured using different  
169 methods, and with differing outcomes (Appendix 2 summarizes the main characteristics of each  
170 dataset as well the findings regarding transcriptional noise obtained in each of the studies). The age  
171 and cell type composition of the final datasets used in our study are shown in Figure 2 - Supplement  
172 1, and the samples included in the datasets as well as the inclusion criteria are provided in Appendix  
173 3. Additionally, the methods implemented in *Decibel* to compute loss of identity were run in parallel  
174 as a control (Figure 2 - Supplement 2). When measuring the *Scallop* membership score of individual  
175 young and old cells to their cell type clusters, the results were inconsistent. Differences between  
176 age groups were found in some datasets, but the directionality of the change was not conserved  
177 across datasets, neither in the average 1 – membership score, nor in the percentage of noisy cells  
178 in the young and the old fraction of each dataset. For most datasets (*Ximerakis et al.*, *Angelidis*  
179 *et al.*, *Martinez-Jimenez et al.*, *Kimmel et al.*), no significant change in mean transcriptional noise  
180 was found. Two datasets (*Enge et al.* and *Salzer et al.*) showed an increase mean membership  
181 associated with aging, although we observed the interquartile range of noise values to be very  
182 similar between young and old individuals. In one of the datasets (*Solé-Boldo et al.*), cells showed  
183 decreased transcriptional noise with aging. Of note, similar inconsistent results were found when  
184 using the preexisting noise-measuring methods as compiled in *Decibel*, even when applying different  
185 methods to the exact same dataset (Figure 2 - Supplement 2). Overall, these results indicated that a  
186 generalized *increase in transcriptional noise* or a *loss of cellular identity* are not universal hallmarks of  
187 aging, at least at the tissue level. However, the possibility that transcriptional noise increased in  
188 specific cell types was still unexplored by these analyses.

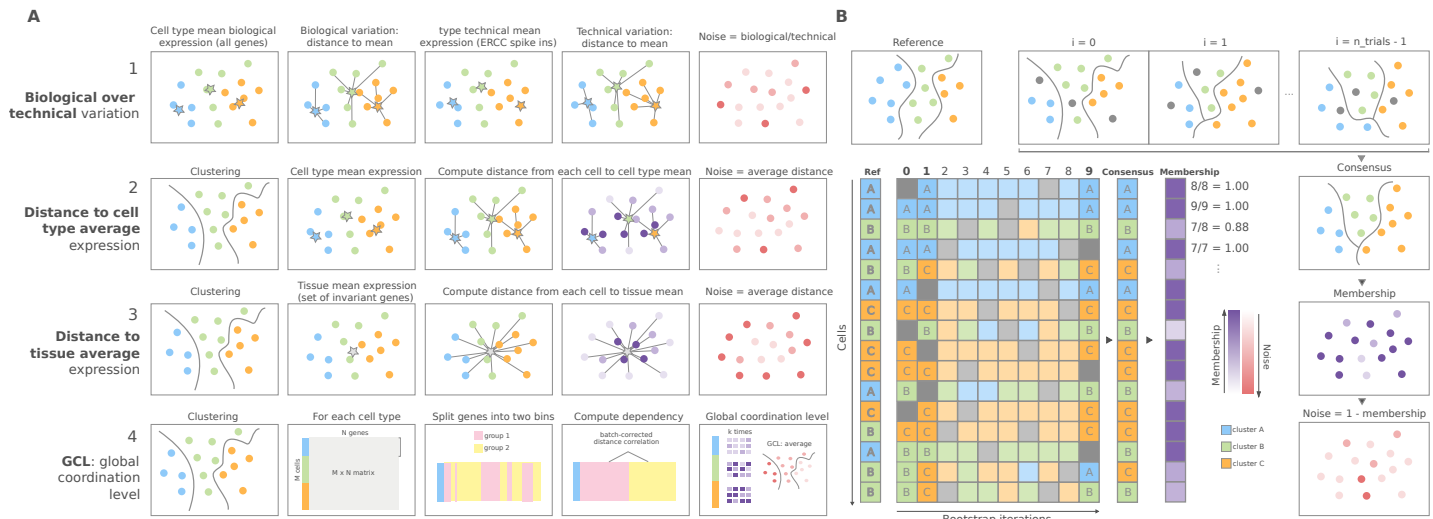


**Figure 1. Overview of computational methods for the quantification of transcriptional noise and example workflow in *Scallop*.** (A) The methods implemented in *Decibel* Python toolkit are summarized through diagrams depicting how they measure transcriptional noise. 1) Biological variation (whole transcriptome-based Pearson's correlation distance between each cell and the mean expression vector), divided by the technical variation (ERCC spike-in based distance) ([Enge et al., 2017](#)) 2) Mean whole transcriptome-based Euclidean distance to cell type average ([Enge et al., 2017](#)) 3) Mean invariant gene-based Euclidean distance to tissue average. ([Enge et al., 2017](#)) 4) GCL ([Levy et al., 2020](#)) per cell type. Stars represent the "center" of each cluster (average gene expression for each cell type). (B) *Scallop*: example workflow on a 16-cell dataset. A reference clustering solution (Ref) is obtained by running a community detection algorithm (default: Leiden) on the whole dataset. Three clusters are obtained: A (blue), B (green) and C (orange). Then, a subset of cells is randomly selected and subjected to unsupervised clustering  $n_{\text{trials}}=10$  times (cells not selected in each bootstrap iteration are shown in grey). The cluster labels across bootstrap iterations are harmonized by mapping the cluster labels with the greatest overlap, using the Hungarian method ([Munkres, 1957](#)). A consensus clustering solution is derived by selecting the most frequently-assigned cluster label per cell, and the membership score is computed as the frequency with which the consensus label was assigned to each cell. *Scallop* measures noise as a  $1 - \text{membership}$  value assigned to each cell.

**Figure 1-Figure supplement 1. Performance of *Scallop* in comparison to preexisting methods for the quantification of transcriptional noise.** The different methods were tested on a dataset of 8,278 human T lymphocytes. (A) UMAPs and dotplot showing *CD3*, *CD4* and *CD8* marker gene expression per cluster. (B) Representation of transcriptional noise levels, as measured by using two distance-to-centroid methods (*euc\_dist* and *euc\_dist\_tissue\_invar*),  $1 - \text{membership}$  (*scallop\_noise*) and Global Coordination Level (GCL). (C) The 10% most stable (purple) and 10% most unstable (red) cells are represented on the UMAP plots for *Euclidean distance to cell type mean* (top row) and *Scallop* methods (bottom row), respectively.

**Figure 1-Figure supplement 2. *Scallop* robustness in relation to input parameters.** The plots on the left show the median correlation distance between membership scores of different runs of *Scallop* against (A) the number of trials, (B) the fraction of cells used in each bootstrap and (C) the resolution given to the clustering method (Leiden) in five independent scRNAseq datasets ([PBMC3K](#), [Joost et al. \(2016\)](#); [Paul et al. \(2015\)](#); [Moignard et al. \(2015\)](#), [Heart10K](#)). The median correlation distance was computed over 100 runs of *Scallop*. The swarmplots on the right show the distribution of the correlation distances between membership scores against each of the input parameters for the heart10k dataset. The median is shown as a red point. While, for the sake of clarity, a random sample of 100 correlation distances is shown for each value of the parameter under study, the median was computed using all the correlation distances. *Scallop* membership scores converge as we increase the number of bootstrap iterations and the fraction of cells used in the clustering.

**Figure 1-Figure supplement 3. Stable cells as identified with *Scallop* are more representative of the cell type than unstable cells.** Distribution of log-fold changes (top row) and adjusted *p*-values (middle row) of the first 100 differentially expressed genes (DEGs) between each cell type or subtype and the rest of the cells in six cell types and subtypes from the 10X PBMC3K dataset. The overlap between the DEGs found when using all of the cells, only the stable cells and only the unstable cells is also shown (bottom row). The adjusted *p*-values obtained with all the cells are equivalent to those obtained using only the most stable half of the cells. In contrast, the differential expression of many genes is not statistically significant when using the unstable half from each population. The overlap between the top 100 DEGs obtained is very high between the stable cells and all cells subsets, whereas DEGs obtained in unstable cells have a very low intersection with all cells.

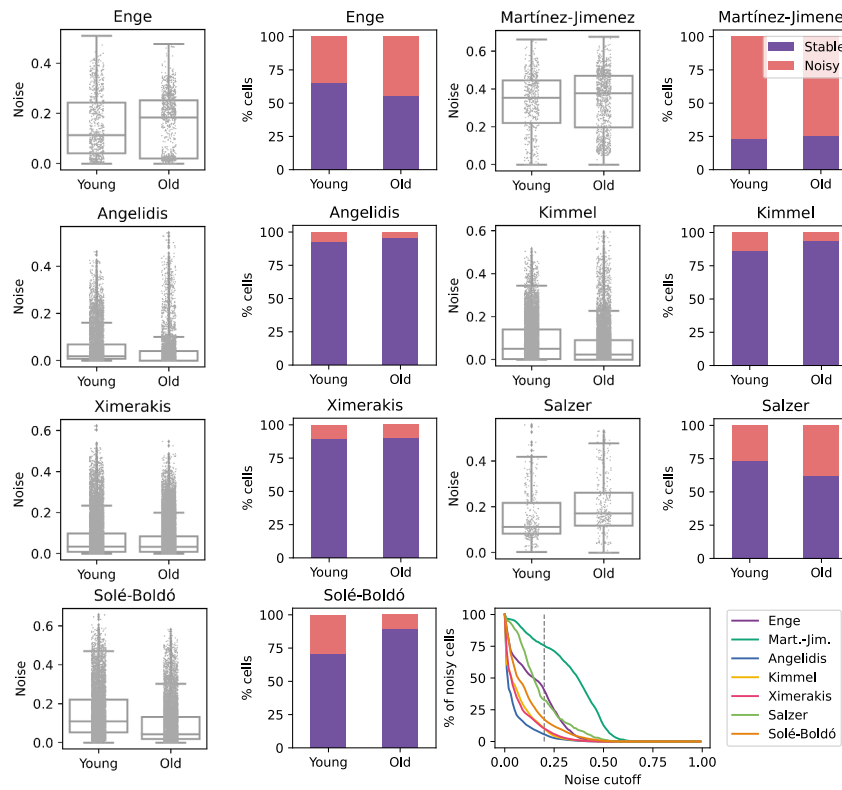


**Figure 2. No consistent increase in transcriptional noise detected in seven scRNASeq datasets of aging at the tissue level.** The graphs show the amount of transcriptional noise, computed as  $1 - \text{membership}$  to cell type clusters, in the young and old age groups of seven single-cell RNAseq datasets of different tissues. For each dataset, the distribution of transcriptional noise values is shown as a stripplot over a boxplot, where the whiskers represent 1.5 times the interquartile range. Next to them the proportions of stable and noisy cells (noise  $\geq 0.2$ ) per age group are shown (Purple bars=stable cells, pink bars=noisy cells). At the bottom right panel, the percentage of noisy cells with a transcriptional noise over a cutoff of 0.2 is plotted against the cutoff. Each colored line represents a different dataset.

**Figure 2-Figure supplement 1. Composition of the seven scRNASeq datasets of aging used in this figure.** UMAPs showing the age and cell type composition of the seven datasets used in the analysis of the age-related transcriptional noise at the tissue level. The UMAPs show the final composition of the datasets used in the experiment. The cell type annotations were obtained from the original authors in all datasets except Kimmel lung, where the labels from Angelidis were projected onto the dataset.

**Figure 2-Figure supplement 2. Measurements of transcriptional noise on seven scRNASeq datasets of aging using computational methods implemented in Decibel.** Stripplots showing the distribution of noise values, as measured by the four alternative methods (Biological variation over technical variation, Euclidean distance to cell type mean, Euclidean distance to tissue mean using invariant genes, and Global Coordination Level - GCL) in the seven datasets used in the analysis of the age-related transcriptional noise at the tissue level. Boxplots and their whiskers represent the interquartile range (IR) and  $1.5 \times \text{IR}$  respectively.

189 **The murine aging lung shows no consistent pattern of transcriptional noise at the  
190 cell type level, and is instead characterized by reproducible alterations in immune  
191 cell composition**

192 Do specific cell types become noisier as they age? In order to answer this question, we focused on  
193 a single tissue and conducted an in-depth analysis of transcriptional noise at the cell type level. For  
194 this, we selected the murine aging lung because of the relative abundance of available datasets in  
195 which authors had reported an age-associated increase in transcriptional noise, yet restricted to  
196 particular cell types: *Angelidis et al.*, *Kimmel et al.*; and the Tabula Muris Senis (TMS) lung droplet  
197 and FACS datasets (*Almanzar et al., 2020*). In each dataset, transcriptional noise was measured as  
198 1 – membership to cell type clusters in the young and old fractions, and the differences in median  
199 noise between the old and the young fraction for each of the existing 31 lung cell types and subtypes  
200 were calculated (Figure 3). Since changes in the gene expression of tissues can also be caused  
201 by altered cell type composition (*Trapnell, 2015*), we estimated the relative abundances of the  
202 31 cell types in the young and old fraction of each dataset and measured the effect of age by  
203 fitting Generalized Linear Models (GLM) to cell type composition data of the four datasets, using  
204 each mouse as a biological replicate (Figure 3 - Supplement 1). By plotting the age-related cell  
205 type enrichment together with the cell-to-cell transcriptional variability in each of the datasets, we  
206 obtained a comprehensive map of cell type enrichment and transcriptional noise associated with  
207 aging at the cell-identity level (Figure 3A). In this analysis, the direction and magnitude of changes in  
208 transcriptional noise varied across cell types. For instance, club cells (a bronchiolar exocrine cell  
209 type) were detected in sufficient numbers in 3 out of 4 datasets, their median membership score  
210 consistently decreasing 10-17% (which showed up as a moderate increase in transcriptional noise  
211 in Figure 3A; bubble #22). Similarly, lung interstitial fibroblasts' transcriptional noise appeared to  
212 increase with age, although with a larger range of membership scores (3-17%; bubble #24). In  
213 both cases, the cell type abundance was not affected by aging. In contrast, alveolar macrophages  
214 showed a decrease in age-associated transcriptional noise (5-12% increase in median membership;  
215 bubble #10). Finally, several cell identities appeared not to change significantly with regard to  
216 their transcriptional noise related to aging. That was clearly the case for capillary endothelial cells  
217 (bubble #9) and plasma cells (bubble #5). Vascular endothelial cells (bubble #6) showed less than  
218 2% of change in noise in 3 out of 4 datasets, but increased up to 8% in one dataset. Therefore, and  
219 contrary to expectation, quantitative analysis of age-associated transcriptional noise did not show a  
220 consistent pattern across diverse lung cell types in the four available datasets.

221 In contrast, the cell abundance analysis did reveal a strikingly consistent enrichment of immune  
222 cell types (lymphocytes in particular) across all datasets in old samples, indicative of immune cell  
223 infiltration in the old tissue. In particular, plasma cells (bubble #5) showed highly consistent enrichment  
224 in old mice, with an Old/Young odds ratio (OR) of 3 in the Kimmel dataset ( $p\text{-value}=1.1 \times 10^{-5}$ )  
225 and of 9.3 in the Angelidis dataset ( $p\text{-value}=6.5 \times 10^{-21}$ ). The ORs for the two TMS datasets were  
226 most likely overestimated due to low cell numbers (only 9 and 22 old plasma cells were detected  
227 in the TMS datasets). The more abundant B cells (bubble #4) were also significantly enriched in  
228 3/4 datasets (Angelidis:  $OR=4.4$ ,  $p\text{-value}=2.5 \times 10^{-69}$ ; Kimmel:  $OR=1.2$ ,  $p\text{-value}=6.3 \times 10^{-8}$ ; TMS  
229 FACS:  $OR=2.0$ ,  $p\text{-value}=8.9 \times 10^{-6}$ ). Other immune cell types such as monocytes, macrophages and  
230 dendritic cells also appeared to be enriched in all datasets. This prompted us to further investigate  
231 the basis for the apparent immune cell enrichment and its potential relationship to increased  
232 transcriptional heterogeneity in the old age. In a qualitative approach to look for consistent pat-  
233 terns across datasets, we ranked cell identities according to their age-related increase in noise  
234 and enrichment (Figure 3 - Supplement 2). While most cell types were evenly distributed along the  
235 transcriptional noise ranking, this representation provided a visible distinction between immune  
236 and non-immune cell types regarding their age-related enrichment, with nearly all immune cell  
237 types appearing on top of the enrichment ranking. For instance, plasma cells (Figure 3 - Supplement  
238 2, #5) were the third most enriched cell type in the Angelidis dataset and appeared on the top

position in the rest of the datasets. Classical monocytes (#13) were found within the top 4 most enriched in 3/4 datasets. Interestingly, natural killer (NK) cells (#2) were the only underrepresented lymphocytes in old mice, and ranked consistently in the least enriched positions among immune cells. Conversely, parenchymal cell types such as goblet cells, club cells and ciliated cells consistently appeared at the bottom of the enrichment ranking, indicating that their proportion diminished with increased immune cell infiltration in the organ or, alternatively, loss of parenchymal cells associated with the old age. Endothelial cells were more evenly distributed along the ranking and thus did not show a clearly discernible age-associated enrichment or loss. Finally, we separated the lung cells into immune and non-immune cell categories and represented transcriptional noise and cell type enrichment values on a heatmap (Figure 3B). As clearly seen in this representation, the transcriptional noise increase associated with aging was extremely variable across cell identities and not always consistent across datasets (a comparison between these results and the results reported by *Angelidis et al.* and *Kimmel et al.* is provided in Figure 3 – 3). In contrast, the immune vs non-immune cell distinction alone explained the behaviour of most cells with respect to their relative abundance with very few exceptions, namely NK cells and alveolar macrophages.

#### Changes in the abundance of the immune and endothelial cell repertoires characterize the human aging lung

Our analysis of age-related cell type enrichment and increase in transcriptional noise in the murine lung highlighted the importance of the changes associated with the relative abundance of cell types that conform the aging lung. To test if this was specific of murine lungs or it could be a more generalized phenomenon, we conducted similar analyses on two large scRNAseq datasets of the aging human lungs (15,852 cells from nine donors from the *Raredon et al.* dataset and 15,048 cells from two donors of the Human Lung Cell Atlas (HLCA) dataset by *Travaglini et al.*; (*Raredon et al., 2019; Travaglini et al., 2020*)). We harmonized cell type labels between datasets by projecting the HLCA labels onto the Raredon dataset (Figure 4 - Supplement 1). Then, we calculated the difference in mean membership score between old and young cells for each cell type in the two datasets, together with the cell type enrichment using the GLM method as described earlier (Figure 4). In general, and similar to what we had previously observed in the murine aging lung, we found a lack of consistency between the two datasets regarding transcriptional noise associated with aging of specific lung cell types. However, we did observe some conserved changes in cell type composition. Particularly, many immune cell types were enriched in older donors, as in the murine aging lung. Plasma cells were significantly enriched in the Raredon dataset (OR=2.6,  $p$ -values=1.9e-6) and enriched, albeit not significantly, in the HLCA dataset (OR=3.5e-11,  $p$ -value=1). The latter result was most probably due to lack of statistical power, as the dataset only consists of two donors. Interestingly, alveolar macrophages were enriched (rather than depleted as in the murine aging lung) in both human aging lung datasets (OR=1.2,  $p$ -value=3.61e-5 in Raredon; OR=2.8,  $p$ -value=1.54e-261 in HLCA). Several endothelial cell types were significantly depleted in the two human aging lung datasets. Vein endothelial cells (OR=0.65,  $p$ -value=7.7e-5 in Raredon; OR=0.58,  $p$ -value=1.9e-9 in HLCA), capillary endothelial cells (OR=0.81,  $p$ -value=3.4e-2 in Raredon; OR=0.3,  $p$ -value=3.5e-141 in HLCA), endothelial cells of lymphatic vessels (OR=0.51,  $p$ -values=1.9e-9 in HLCA). These results indicated that aged human lungs present reduced vascularization and significant immune cell infiltrates as compared to the young. These facts may have influenced previous analyses of transcriptional noise associated with aging.

#### Distance-to-centroid methods detect transcriptionally stable cell subtypes as transcriptional noise

A relevant open question is what was the source of apparent transcriptional *noise* in previous studies that were based on distance-to-centroid methods. Since we found important changes in the community of human alveolar macrophages in the HLCA dataset, we conducted an in depth analysis on that cell type that revealed four distinct alveolar macrophage communities that emerge with

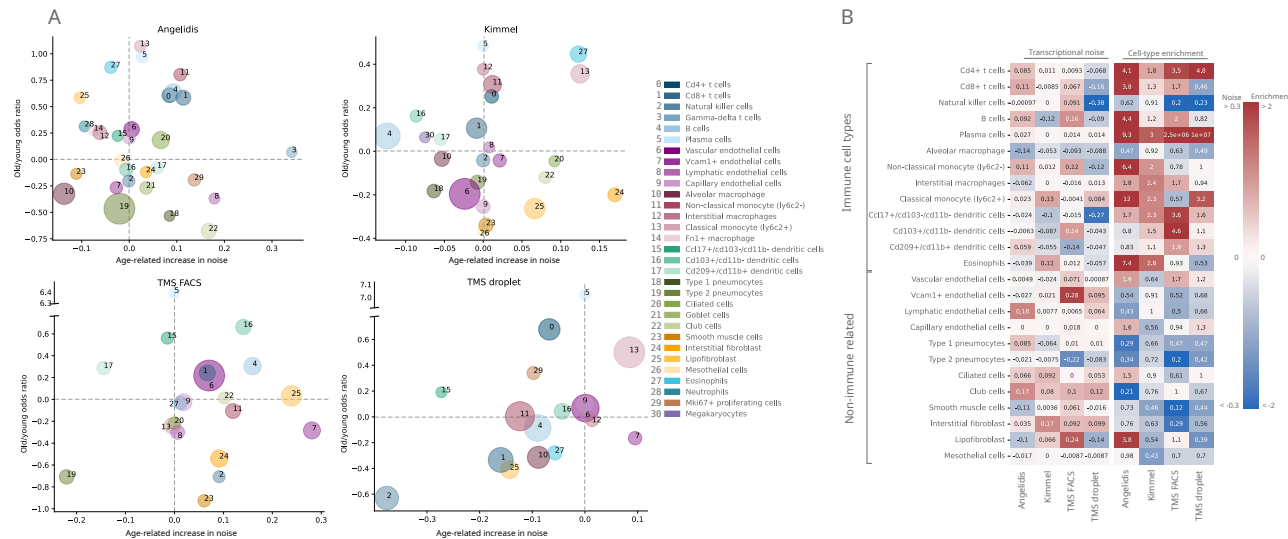


**Figure 3. Lack of evidence for an increase in transcriptional noise of the murine aging lung and detection of an enrichment in immune cells.** (A) Bubble chart of transcriptional noise and cell type enrichment (old/young OR) of 31 murine lung cell identities. The age-related change in transcriptional noise (horizontal axis) is computed by *Scallop* as the decrease in median membership score per cell identity between young and old cells. The enrichment of each cell type in old samples with respect to their young counterpart is represented as the old/young OR (vertical axis). The area of the bubbles represents the expected proportion of each cell type in the whole dataset according to the binomial GLM fitted for that dataset. (B) Immune cell type enrichment, but not age-associated increase in transcriptional noise, is consistently detected in old mice lungs. The increase in transcriptional noise associated with aging (left) and the cell type enrichment (right) are shown for several lung cell identities classified on the left as immune and non-immune. Cell identities present in at least 3 out of the 4 studied datasets are shown, and the age-related difference in transcriptional noise of missing cell identities is imputed from the remaining three measurements (mean difference across datasets).

**Figure 3–Figure supplement 1. Composition of the four scRNAseq datasets of the murine aging lung used in this figure.** (a) Experimental approach. Four murine aging lung datasets were preprocessed and cell type-annotated. The cell-type labels from Angelidis were used as a reference to annotate the rest of the datasets. Differences in cell-type abundance between young and old mice were quantified using GLMs. From each dataset, eight subsets of related cell-types were created to classify the 31 cell types into 8 categories, which were used as input for *Scallop* to analyze the differences in cell-to-cell variability. (b) Cell type-annotated mouse lung datasets. UMAP plots showing the four datasets with their cell type annotations.

**Figure 3–Figure supplement 2. Qualitative ranking of murine aging lung cell types according to transcriptional noise and cell type enrichment.** The 31 detected lung cell types were classified in the *Noise* ranking (left) according to their greater age-related increase in noise. They were also classified in the *Enrichment* ranking (right) according to their greater enrichment in old samples. Cell categories that were represented by fewer than 100 cells were excluded from the transcriptional noise evaluation, and therefore do not appear in the plot. Specific cell types are shown in the same color and with the same numbers as specified in the legend.

**Figure 3–Figure supplement 3. Comparison of the originally reported cell type-associated increase in transcriptional noise with the results obtained with *Scallop*.** The content of the first three columns was drawn from the original publications (*Angelidis et al.*; *Kimmel et al.*). More specifically, *Angelidis\_TN* is the transcriptional noise per cell identity on the Angelidis dataset (from their figure 2); *Kimmel\_OD* is the gene overdispersion per cell type on the Kimmel dataset (from their figure 2B); and *Kimmel\_DC* is the cell-cell heterogeneity per cell identity measured as the Euclidean distance to the centroid of the cell identity for a particular age. Columns 4-7 summarize the results of our analysis of age-related loss of cell type identity in the murine lung. Specifically, *Angelidis\_S*, *Kimmel\_S*, *TMS\_FACS\_S* and *TMS\_drop\_S* report the transcriptional noise per cell identity on the four datasets, measured as the difference in median membership score between young and old individuals. The cell identities used are those drawn from Angelidis. Since some cell identities from Kimmel dataset did not have a 1:1 correspondence to the Angelidis cell identities, they are shown using their original notation at the bottom of the table ("Additional cell identities"). UP/DOWN: age-related increase/decrease in noise, NS: the difference in noise between young and old individuals is not statistically significant. NP: the cell identity was not present in the dataset in sufficient amounts to perform the analysis. For most cell types, it can be concluded that there is little overlap between cell identity-specific noise measurements across datasets and methods

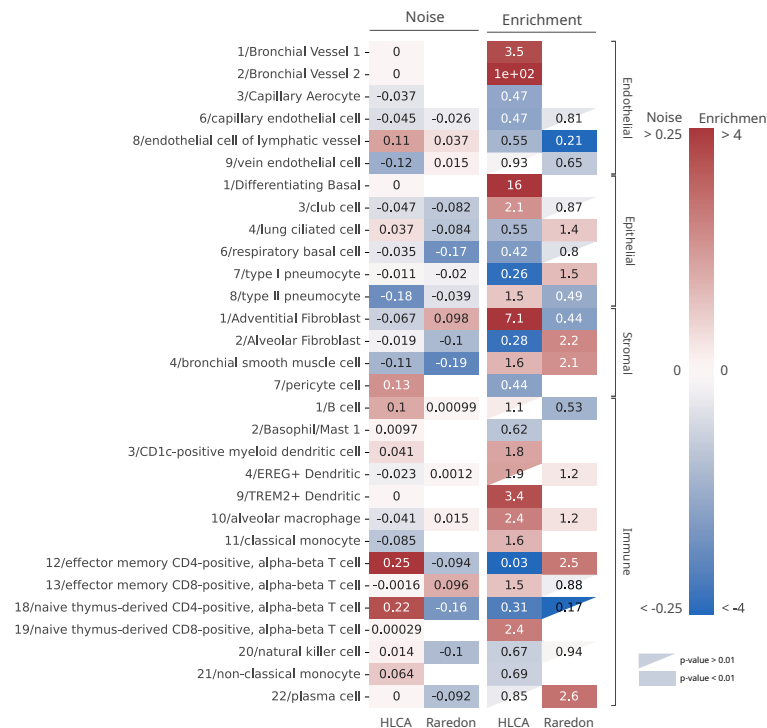


**Figure 4. Human aging lungs show no increase in transcriptional noise but consistent depletion and enrichment of specific endothelial and immune cell types.** The increase in transcriptional noise associated with aging (Noise, left) and the cell type enrichment (Enrichment, right) values are shown for 30 human lung cell identities as detected in the HLCA and Raredon datasets ([Raredon et al., 2019](#); [Travaglini et al., 2020](#)). For each cell type, its age-related increase in noise (difference in  $1 - \text{membership}$  between old and young individuals per cell type) and the Old/Young OR are shown. Only cell types whose enrichment/depletion are statistically significant in at least one of the datasets are shown, and the ORs associated with a  $p$ -value  $> 0.01$  are shown as a triangle. The color-bar for the enrichment is shown in a logarithmic scale.

**Figure 4–Figure supplement 1. Composition of the two scRNAseq datasets of the human aging lung used in this figure.** The UMAP plots with the age and cell type identity annotations are shown for each tissue compartment (endothelial, epithelial, stromal and immune) and each dataset separately.

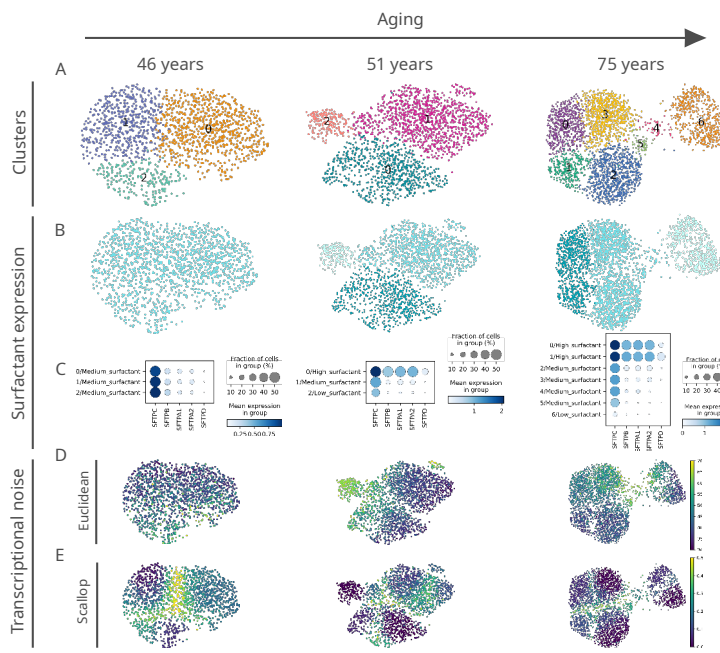


**Figure 5. Euclidean distance-to-centroid methods are unable to distinguish *bona fide* transcriptional noise from alternative cell fate specification.** (A) An increasing number of alveolar macrophage subclusters (as obtained with Leiden) are detected in three donors (aged 46, 51, and 75 years) from the *Travaglini et al.* (HLCA) dataset. (B-C) The new cell clusters are characterized by differential surfactant protein gene expression levels, as clearly seen on the UMAP (B) and dotplot (C) representations. (D-E) Transcriptional noise measurements, using the Euclidean distance to cell type mean (D) and  $1 - \text{membership}$  using *Scallop* (E), demonstrate that only the latter method is able to distinguish *bona fide* transcriptional noise from the formation of new clusters that are transcriptionally stable.

**Figure 5-Figure supplement 1. Expression of surfactant protein genes by human alveolar macrophages.**

Differential expression by alveolar macrophage cell clusters of the genes coding for surfactant proteins *SFTPA1*, *SFTPA2*, *SFTPB*, *SFTPC*, and *SFTPD* is shown for three donors (aged 46, 51 and 75) of the *Travaglini et al.* (HLCA) dataset.

aging from a single transcriptionally homogeneous cluster (see Figure 5 and Supplement 1). The four aged alveolar macrophage subclusters present a markedly different expression of genes coding for surfactant proteins (*SFTPA1*, *SFTPA2*, *SFTPB*, *SFTPC*, and *SFTPD*), i.e. they show changes consistent with alternative fate determination. Deregulated surfactant protein expression is connected to the age-related functional decline of human lungs. In fact, mutations in the gene coding for surfactant protein C (*SFTPC*) and in the *MUC5B* promoter region are linked to pulmonary fibrosis, but the effects of these mutations are usually not observed until late in life (around 60-70 years old), because age-related decline in proteostasis is needed for aggregation prone or misfolded proteins to actually cause damage (*Schneider et al., 2021*). Interestingly, we measured the age-associated transcriptional noise in the alveolar macrophage community using a distance-to-centroid method (*Euclidean distance to the cell type mean*) and *Scallop*, and observed that only the latter algorithm could accurately detect the emergence of distinct and transcriptionally stable alveolar macrophage subpopulations, whereas the distance-to-centroid method would interpret this specification of alternative cell fates as a single macrophage population undergoing loss of identity (Figure 5).

**Discussion**

Mechanistically, it is not clear if aging is a tightly regulated process or may be the result of passive phenomena of stochastic nature (*Schmeer et al., 2019; Gladyshev, 2016; Costa et al., 2016*). In the absence of further mechanistic insight, aging is characterized by a series of phenotypic changes at

306 the cellular and tissue levels, such as genomic instability, epigenetic alterations, chronic low level  
307 inflammation (*inflammaging*), immunosenescence, and impaired regeneration (*López-Otín et al., 2013; Gems and de Magalhães, 2021*). In addition, an increase in transcriptional noise has been  
308 observed in some aged tissues and cell types (*Enge et al., 2017; Martinez-Jimenez et al., 2019; Angelidis et al., 2019; Kimmel et al., 2019*). Transcriptional noise could be related to genomic instability  
309 (*Vijg, 2021*), epigenetic deregulation (*Lu et al., 2020b; Oliviero et al., 2022*) or loss of proteostasis  
310 (*Li et al., 2020*), all established hallmarks of aging. Some authors consider transcriptional noise to  
311 be a hallmark of aging in and of itself (*Mendenhall et al., 2021*). Since aging is multifactorial and  
312 mutational load most likely leads to clonal expansion of aberrant cells that accumulate throughout  
313 the lifetime of the individual, other authors suggest that aging traits may be associated with cell type  
314 imbalance in aged organs (*Cagan et al., 2022*). Another recent hypothesis is *inter-tissue convergence*  
315 through age-associated loss of specialization (*Izgi et al., 2022*).

316 In this work, we made a systematic comparison of the most important families of methods  
317 that have been used to quantify age-related transcriptional noise through the implementation of  
318 *Decibel*, a novel Python toolkit. Since we were not convinced of the utility of these methods to  
319 determine *bona fide* transcriptional noise, we developed a novel method and applied it to a wide  
320 array of tissues. Our proposed tool, *Scallop*, presents some advantages over existing methods: it  
321 does not require neither ERCC spike-ins nor cell type labels. In addition, it provides information  
322 that is complementary to the GCL, as it yields a cell-wise measurement of transcriptional noise that  
323 enables us to compare between *stable* and *unstable* cells within the same cluster or cell type. Most  
324 importantly, *Scallop* measures transcriptional noise by membership to cell type-specific clusters  
325 which is a re-definition of the original formulation of *noise* by *Raser and O'Shea*. This is in stark  
326 contrast to measurements of *noise* including other phenomena (as demonstrated in Figure 5) by  
327 the distance-to-centroid methods prevalent in the literature. When applied to seven independent  
328 aging datasets, the results obtained revealed little overlap in the magnitude and directionality of the  
329 changes in transcriptional noise associated with aging of the different tissues analyzed, providing  
330 evidence that an increase in transcriptional noise might not be as evident as generally thought.

331 In order to investigate cell type-specific effects in transcriptional noise, it is crucial to compare  
332 between different datasets of the same aging tissue. Otherwise, it is difficult to ascertain whether  
333 the variability observed between cell types is due to a pattern that is conserved in that tissue or is  
334 merely the effect of the intrinsic variability associated with scRNAseq experiments (*Fonseca Costa et al., 2021*). For the cell type-specific study, we focused on the aging lung, as the effect of aging  
335 of this tissue has gained relevance (*Schiller et al., 2019*) due to its association with chronic  
336 obstructive pulmonary disease (COPD), lung cancer and interstitial lung disease (*Angelidis et al., 2019; Schneider et al., 2021*), and its increased risk of severe illness in COVID-19 patients (*Williamson et al., 2020*). In the 31 cell types analyzed in mouse lungs, we found increased transcriptional noise  
337 in club cells and interstitial fibroblasts only, while alveolar macrophages seemed to decrease it. Of  
338 interest, a single-cell analysis of alveolar macrophages did not identify distinct clusters associated  
339 with mouse or human aging, identifying changes in the aged alveolar microenvironment as key for  
340 their altered functionalities (*McQuattie-Pimentel et al., 2021*). In humans, we analyzed two aging  
341 lung datasets that provide complementary information, as the final Raredon dataset consists of 9  
342 donors of a wider range of ages but is not as well-powered in terms of cell type resolution as the  
343 HLCA dataset, which contains 48 cell identities. Similar to what we had previously observed in the  
344 murine aging lung, there was no consistency between the two datasets regarding transcriptional  
345 noise of the 30 specific cell types detected. However, both in human and mouse lungs we detected  
346 a shift in the abundance of a number of cell populations with age, most clearly seen for immune  
347 cells.

348 In fact, the age-associated increase in immune cell infiltration of solid organs may be generalized.  
349 Specifically, one study found neutrophil and plasma cell infiltration in adipose tissue, aorta, liver  
350 and kidneys of aged rats of both sexes, and the immune cell infiltration was reversed by caloric  
351 restriction (*Ma et al., 2020a*). Another study found a subtype of highly secretory plasma cells

357 infiltrated in the aged bone marrow, spleen, fat, kidney, heart, liver, muscle, and lungs (*Schaum*  
358 *et al., 2020*). Of note, immune cell senescence has been shown to induce aging of solid organs  
359 (*Yousefzadeh et al., 2021*), in what has been proposed to be a feed-forward circuit (*Salminen, 2021*).  
360 Therefore, the importance of immune cell infiltration of the aged lungs cannot be overlooked. In fact,  
361 age-associated immune cell type enrichment has also been observed in two independent studies  
362 of macaque lungs. One study found increased mast cells, plasma cells and CD8+ T cells in aged  
363 lung tissue (*Ma et al., 2020b*), while the other found increased alveolar and interstitial macrophage  
364 numbers in bronchoalveolar lavages of old macaques (*Rhoades et al., 2022*). The significance of the  
365 shift in cellular composition of the aged lungs in relation to the appearance of aging traits remains  
366 to be determined. Of note, alternative explanations for transcriptional changes associated with  
367 aging such as *tissue convergence* are compatible with shifts in the cellular composition of aging  
368 tissues and organs being a primary cause of convergence (*Izgi et al., 2022*).

369 In summary, the sources of the apparent increase in *transcriptional noise* reported by previous  
370 studies may be multiple, and are mostly related to the computational methods used to characterize  
371 transcriptional noise and cellular identity in aged tissues. Open availability of *Decibel* and *Scallop*  
372 represents an opportunity for the aging research community to further investigate these issues,  
373 and they are also valuable for researchers addressing cell-to-cell variability of scRNAseq datasets in  
374 other settings.

## 375 Methods

### 376 **Decibel: Python toolkit for the quantification of transcriptional noise**

377 We developed a Python toolkit for the quantification of loss of cell type identity associated with  
378 aging. We implemented methods as they were originally described in the literature.

#### 379 Biological variation over technical variation

380 Biological variation over technical variation is measured as in the original formulation by *Enge et al.*,  
381 by computing  $1 - \rho$ , where  $\rho$  is the Pearson's correlation between the gene expression vector of  
382 each cell and the mean expression of its cell type, i.e., the gene expression averaged over all the  
383 cells from the same cell type and individual. For each cell type and individual mouse or donor, the  
384 mean gene expression vector – the averaged expression of the whole set of monitored genes across  
385 cells – is computed. Then, the biological variation is measured as the Euclidean distance from each  
386 cell to its cell type mean for that individual. The technical variation is computed using the same  
387 procedure, but using only the ERCC spike-ins in the calculation of the distance to cell type mean.  
388 Finally, the transcriptional noise is calculated by dividing the biological variation by the technical  
389 variation per cell.

#### 390 Euclidean distance to cell type mean

391 The distance to the cell type mean is measured as the second method described by *Enge et al.*.  
392 For each cell type and individual mouse or donor, we compute the average whole-transcriptome  
393 expression. The noise is quantified as the Euclidean distance between the gene expression vector  
394 of each cell and its corresponding individual-matched cell type mean expression vector.

#### 395 Invariant gene-based Euclidean distance to tissue mean

396 This is the third method described by Enge et al. (*Enge et al., 2017*). It is computed as the Euclidean  
397 distance from each cell to the average expression across cell types using a pre-selected set of  
398 invariant genes that is selected as follows: first, genes are sorted according to their mean expression  
399 and split into 10 equally sized bins, and the two extreme bins are discarded (10% most expressed  
400 and 10% least expressed genes). Then, the 10% of genes with the lowest coefficient of variation  
401 within each bin are selected and used for the calculation of the Euclidean distance between the  
402 mean expression vector across cell types and each of the cell expression vectors.

403    Average Global Coordination Level

404    Taking the Matlab code provided by the authors, we implemented the GCL in Python. As the  
405    original formulation was used in datasets with a single cell type, here we computed the GCL for  
406    each cell type separately and then calculated the average GCL for the tissue. For each cell type, the  
407    GCL was calculated by splitting the whole transcriptome into two random halves and computing  
408    the batch-corrected distance correlation between them (*Levy et al., 2020*). The GCL per cell type  
409    was averaged over k times. Following the authors' recommendation, we used k=50 in all of our  
410    calculations.

411    **Scallop**

412    *Scallop* iteratively runs a clustering algorithm of choice on randomly selected subsets of cells. Then,  
413    it computes the frequency with which each cell is assigned to the most frequently assigned cluster.  
414    *Scallop* has three key steps: 1) Bootstrapping, 2) Mapping between cluster labels across bootstrap  
415    iterations, and 3) Computation of the membership score.

416    Bootstrapping

417    *Scallop* runs a community-detection algorithm (default: Leiden (*Traag et al., 2019*)) on subsets of  
418    cells drawn from the original dataset. The subsets are selected randomly with replacement from  
419    the whole population (the seed can be defined by the user). The number of cells to be selected  
420    on each bootstrap iteration is computed through the fraction of cells user-defined parameter  
421    `frac_cells` (default: 0.95). The community detection algorithm is run `n_trials` times (default:  
422    30). An additional clustering is run with all the cells (`frac_cells=1`) for it to be used as a reference  
423    in the mapping stage. A bootstrap matrix (`n_cells × n_trials`) is obtained that contains the  
424    cluster labels that have been assigned to each cell on each bootstrap iteration. The cluster labels  
425    are the ones obtained from the python implementation of Leiden through the `Scanpy` function  
426    `sc.tl.leiden()` and are numbered from '0' to  $n$  according to the size of the cluster, i.e., the cluster  
427    with the highest number of cells is assigned the label '0', the second most abundant is assigned the  
428    label '1', and so on. Since the subset of cells used in each run is different, clustering results vary  
429    from run to run and labels are not comparable between bootstrap iterations.

430    Cluster relabeling

431    In order to compare between cluster assignments from different bootstrap iterations, cluster  
432    identities need to be relabeled. A contingency table is computed between each clustering solution  
433    in the bootstrap matrix and a reference clustering, which was obtained by running the community  
434    detection algorithm on all the cells. From the original bootstrap matrix, we obtain a relabeled  
435    bootstrap matrix. The assumption is made that if cluster A from bootstrap iteration  $i$  and cluster  
436    B from bootstrap iteration  $j$  have a large number of cells in common, then they should have the  
437    same label. In order to find the mapping between clusters, an overlap score matrix is computed for  
438    every column in the bootstrap matrix against the reference labels. The overlap score ( $S$ ) between  
439    cluster A from the reference clustering solution ( $A_{ref}$ ) and cluster B from the  $i$ -th iteration ( $B_i$ ) is  
440    defined as follows:

$$S(A_{ref}, B_i) = \frac{|A_{ref} \cap B_i|}{|A_{ref}|} + \frac{|A_{ref} \cap B_i|}{|B_i|}$$

441    Where  $|A_{ref}|$  and  $|B_i|$  are the number of cells in the cluster A and B from the reference clustering  
442    solution and the  $i$ -th bootstrap iteration, respectively, and  $|A_{ref} \cap B_i|$  is the number of cells in  
443    common between the two clusters. The score is then [0-1]-scaled by dividing it by the maximum  
444    score: 2. The maximum score would correspond to a total overlap between the two clusters.

445    The score is computed for every pair of clusters between the reference solution and each of  
446    the bootstrap iterations to obtain a contingency matrix ( $n_{clusters_{ref}} \times n_{clusters_i}$ ). In order to find  
447    the optimal mapping between the two clustering solutions, we search for the permutation of the

448 columns that maximizes the trace of the contingency matrix. We do this by using Munkres, a Python  
449 implementation of the Hungarian method (*Munkres, 1957*).

450 As the reference clustering solution is computed on the whole dataset but each of the bootstrap  
451 iterations is run on a subset of cells (*frac\_cells*), the number of clusters obtained in each iteration  
452 might not be equal to the number of clusters in the reference. In order to deal with this, we consider  
453 three cases:

- 454 1. The number of clusters in the reference clustering solution is equal to the number of clusters  
455 obtained in the *i*-th bootstrap iteration. This case is dealt with easily, as the Hungarian method  
456 yields a 1:1 mapping between the two clustering solutions.
- 457 2. Fewer clusters are obtained in the *i*-th bootstrap iteration than in the reference solution. This  
458 may happen if one or more clusters from the reference are merged into a single cluster in a  
459 bootstrap iteration. In this case, a 1:1 mapping is obtained, but one or more of the cluster  
460 labels from the reference clustering remain unused.
- 461 3. More clusters are obtained in the *i*-th bootstrap iteration than in the reference solution. This  
462 may happen if one cluster from the reference is further divided into two or more subclusters in  
463 a bootstrap iteration. A 1:1 mapping is obtained, but one or more clusters from the bootstrap  
464 iteration remain unmapped. Usually, this means than a cluster from the reference solution  
465 was divided into two or more subclusters in the bootstrap iteration. In this case, the subcluster  
466 with the largest overlap degree with one of the clusters in the reference clustering solution,  
467 receives its label. The other subcluster remains unmapped. When this happens, those clusters  
468 are flagged as *unmapped* until the end of the bootstrapping process. Then, an additional  
469 mapping step is carried out between the *unmapped* clusters from all bootstrap iterations.  
470 This is done by creating an overlap score matrix similar to the one created in the mapping  
471 process and searching for the permutation of the columns that maximizes its trace, using  
472 the Hungarian method. In order to avoid spurious mappings between unrelated *unmapped*  
473 clusters, a minimum overlap score of 0.1 is imposed for two *unmapped* clusters to be renamed  
474 as the same cluster.

475 **Computation of the membership score**

476 *Scallop* computes three different membership scores: a frequency score ('freq'), an entropy score  
477 ('entropy') and a Kullback-Leibler divergence score ('KL'). We use the frequency score here as it  
478 yields results that are consistent to the ones obtained with the other two alternative scores, and  
479 its meaning is more intuitive than those of the two alternative methods. The frequency score is  
480 computed as the fraction of bootstrap iterations where a cell was assigned to the most frequently  
481 assigned cluster label. In order for the score to take values between 0 and 1, only the cells selected in  
482 each bootstrap run are considered as the total number of cells. More information on the calculation  
483 of the entropy and the Kullback-Leibler scores can be found in the *Scallop* documentation.

$$\text{Freq score} = \max \left\{ \frac{|c_i|}{\sum_{j \in \text{clusters}} |c_j|} \mid i \in \text{clusters} \right\}$$

484 **Validation of Scallop**

485 In order to validate our method for transcriptional noise quantification, we conducted three analyses:  
486 1) we graphically evaluated the output of *Scallop* on a dataset of human T cells, 2) we analyzed  
487 its robustness to input parameters, and 3) we studied the relationship between membership and  
488 robust marker expression, using a PBMC dataset.

489 **Stable and unstable cells in the 8K human T cells**

490 We downloaded a [23,766 PBMC](#) dataset from from 10X Genomics. We ran the standard processing  
491 pipeline including highly variable gene detection, dimensionality reduction through PCA and UMAP,  
492 and clustering. We annotated the dataset according to PBMC marker expression and selected the

493 cluster of T lymphocytes. We obtained a dataset of 8,278 cells. We ran the processing pipeline on  
494 the T lymphocyte dataset and obtained three main clusters of cells, which we annotated as *0/CD4+*  
495 *T cells*, *1/CD4+ T cells* and *2/CD8+ T cells* according to their expression of the gene markers *CD3C*,  
496 *CD3D*, *CD3E*, *CD4*, *CD8A* and *CD8B*. Then, we calculated the whole transcriptome-based Euclidean  
497 distance to the cell subtype mean (*euc\_dist*), the invariant gene-based Euclidean distance to the  
498 T cell mean (*euc\_dist\_tissue\_invar*), the *Scallop* noise as 1-membership (*scallop\_noise*) and the GCL  
499 per T subtype. We selected the 10% most stable and 10% most unstable cells as those having the  
500 lowest and highest noise scores according to two methods: *euc\_dist* and *scallop\_noise*.

501 **Robustness to input parameters**

502 We selected a set of five scRNAseq datasets of various sizes and depths (Table 1). Three datasets  
503 were taken from published scRNAseq studies (*Paul et al., 2015; Moignard et al., 2015; Joost et al.,  
504 2016*) and two were from 10X Genomics (*PBMC3K, Heart10K*). We computed the membership  
505 scores of all the cells in five datasets 100 times, on a range of bootstrap iterations (*n\_trials*),  
506 fraction of cells used in each iteration bootstrap (*frac\_cells*) and resolution (*res*) values. We  
507 then computed the median correlation distance between the 100 runs of *Scallop* with each set of  
508 parameters. We used the *spatial.distance.correlation* method from Scipy to compute the  
509 correlation distance.

510 **Statistical significance of differential expression of PBMC markers**

511 The assessment of the cell-to-cell variability associated with aging using *Scallop* relies on the assumption  
512 that cell-to-cell variability is caused by transcriptional noise, and that it can be measured by  
513 evaluating cluster stability. We checked our assumption by comparing the transcriptomic profiles of  
514 the cells that had a high and a low membership score (measured using *Scallop*). *Stable* cells should  
515 have a more robust expression of cell type markers than the *unstable* cells. We downloaded the  
516 *PBMC 3K dataset* from 10x Genomics. After running the standard processing pipeline, we ran  
517 *Scallop* on the dataset and selected the most stable and most unstable half of the cells within each  
518 annotated cluster. For each cell type, we defined the most stable cells as those with a membership  
519 score greater than the median membership score of that cell type. Hence, we compared two sets of  
520 cells (stable vs unstable) of the same size and we analyzed the effect size and statistical significance  
521 of a routine downstream analysis (differential expression) when given each of the sets as input.  
522 We computed the 100 most differentially expressed genes (DEGs) between each cell type and the  
523 rest of the cells using 1) all cells, 2) only the stable cells and 3) only the unstable cells. B cells and  
524 megakaryocytes were excluded from the analysis as the former were highly stable (so we could not  
525 compare between the stable and the unstable fraction) and the latter consisted of very few cells.  
526 We compared the distribution of log-fold changes and *p*-values associated with those DEGs when  
527 using only the stable, only the unstable and all the cells.

528 **Single-cell RNA sequencing data processing**

529 **2,5K human aging pancreatic cells**

530 The raw count matrices and the metadata files from *Enge et al.* were downloaded from the Gene  
531 Expression Omnibus (accession number: [GSE81547](https://www.ncbi.nlm.nih.gov/geo/query/acc.cgi?acc=GSE81547)). The separate GSM files were merged into a  
532 single raw count matrix and processed them using the following pipeline in Scanpy (*Wolf et al., 2018*):  
533 filtering of low quality cells and genes, normalization, log-transformation of counts, PCA, batch-effect  
534 correction using harmony (*Korsunsky et al., 2019*), Leiden community detection (resolution=1.0)  
535 and UMAP dimensionality reduction. 11 clusters were obtained and annotated using the expression  
536 of the markers *INS* ( $\beta$  cells), *GCG* ( $\alpha$  cells), *SST* ( $\delta$  cells), *PRSS1* (acinar cells), *PROM1* (ductal cells), *PPY*  
537 (PP cells) and *THY* (mesenchymal cells). Donors were classified into three categories as in the original  
538 work by *Enge et al.*: "pediatric" (0-6 years old), "young" (21-22 years old) and "old" (38-54 years old).  
539 Samples from pediatric donors were not used in the aging analysis (see Inclusion Criteria 3).

540 1,5K murine aging CD4+ T cells

541 We downloaded the raw data and metadata files from (*Martinez-Jimenez et al., 2019*) from the  
542 authors' [GitHub](#). We created an annData object with the raw count matrix and the metadata  
543 (mouse strain, age-group, stimulus, individual and cell type). We identified and flagged the counts  
544 corresponding to ERCC spike-in controls. We ran a standard processing pipeline: filtering out low  
545 quality cells and genes, normalization and log-transformation of counts, selection of highly variable  
546 genes, batch-effect correction between mouse strains (*Mus musculus domesticus* and *Mus musculus*  
547 *castaneus*) and dimensionality reduction was conducted (PCA and UMAP).

548 14,8K murine aging lung cells

549 We downloaded the raw count matrix and the metadata file from (*Angelidis et al., 2019*) from the  
550 Gene Expression Omnibus (accession number: [GSE124872](#)). We created an annData object with the  
551 raw count matrix and the available metadata (cell type annotation, age group, cluster and mouse).  
552 We ran a standard processing pipeline: quality control, normalization and log-transformation of  
553 counts, selection of highly variable genes, batch-effect correction between individual mice using  
554 bbknn (*Park et al., 2018*) and dimensionality reduction (PCA and UMAP). In our analysis, we used  
555 the cell type annotations provided by the authors. We also annotated the rest of the murine aging  
556 lung datasets using their annotation as a reference. In order to do that, we computed the DEGs  
557 between each lung cell type and the rest of the dataset to obtain a set of gene markers for each  
558 cell type. We then used those markers to annotate the rest of the datasets using scoreCT (*Seninge,*  
559 *2020*).

560 90,6K murine aging lung, spleen and kidney cells

561 We downloaded the raw count matrices and the metadata files from *Kimmel et al.* from the Gene  
562 Expression Omnibus (accession number: [GSE132901](#)). We selected lung samples (30,255 cells) and  
563 excluded kidney and spleen samples. We discarded the two samples from the individual Y1, as  
564 they showed a very different count distribution to the rest of the samples (see Appendix 4). We  
565 created an annData object with the count matrix and the metadata (sample, tissue, age, mouse).  
566 We ran a standard processing pipeline: quality control, normalization and log-transformation of  
567 counts, highly variable gene selection, batch-effect correction between individual mice using bbknn  
568 (*Park et al., 2018*), dimensionality reduction (PCA and UMAP) and Leiden clustering (*Traag et al.,*  
569 *2019*) with high resolution value (resolution = 4), so that we obtained a very granular clustering  
570 solution. We obtained 52 clusters and we annotated them by projecting the cell type identity labels  
571 from the *Angelidis et al.* dataset, using the automated cell type annotation tool scoreCT (*Seninge,*  
572 *2020*). We checked that cells clustered primarily according to their cell type, meaning no important  
573 batch effects were present in the final datasets, and that clusters expressed the cell type markers  
574 expected according to their assigned cell type labels (see Appendix 5).

575 731 murine aging dermal fibroblasts

576 The count matrix and metadata from *Salzer et al.* were downloaded from the Gene Expression  
577 Omnibus (accession number: [GSE111136](#)). A standard processing pipeline (quality control, normal-  
578 ization, log-transformation, HVG detection, PCA, neighbor computation and UMAP dimensionality  
579 reduction) was applied to the dataset.

580 22,1K human aging skin cells

581 We downloaded raw count matrices from *Solé-Boldo et al.* from the Gene Expression Omnibus  
582 (accession number: [GSE130973](#)). We ran a standard preprocessing pipeline on the count matrix:  
583 quality control, normalization, log-transformation, HVG detection, PCA, neighbor computation and  
584 UMAP dimensionality reduction. We used the original cell type labels provided by the authors.

585 Tabula Muris Senis lung datasets

586 The 3,2K TMS FACS-sorted and the 4,4 TMS droplet lung cell datasets were downloaded from [figshare](#).  
587 A standard preprocessing pipeline was run on the two datasets, and cluster labels were harmonized  
588 with the rest of the murine aging lung datasets by using the genes differentially expressed between  
589 cell types from the Angelidis dataset as input for the automated cell-type annotation through  
590 scoreCT ([Seninge, 2020](#))

591 Human Lung Cell Atlas

592 We downloaded the full lung and blood 10X dataset from the HLCA ([Travaglini et al., 2020](#)) from  
593 Synapse (ID: [syn21041850](#)). The original dataset consists of lung samples from 3 patients: a 46  
594 years old male donor (donor 1), a 51 years old female donor (donor 2) and a 75 years old male  
595 donor (donor 3). The composition of the samples was not equivalent across donors: there were two  
596 samples from donor 1 (distal and medial), three samples from donor 2 (blood, distal and proximal)  
597 and two samples from donor 3 (blood and distal). Thus, we selected the distal sample from the  
598 three donors and obtained a dataset of 18,542 cells from donor 1, 16,903 cells from donor 2 and  
599 7,524 cells from donor 3. We subsampled 7,524 cells from each of the donors in order to correct  
600 for the age-group imbalance, and obtained a dataset of 22,572 lung cells. We used this balanced  
601 dataset of distal samples from the three donors to create two datasets. On the one hand, we  
602 selected all lung cells from donors 1 and 3 (46 years old and 75 years old, all male) in order to create  
603 the 15,048 aging lung cell dataset used in the noise and enrichment analysis. On the other hand,  
604 we selected all alveolar macrophages from the three donors in order to create the 11,484 alveolar  
605 macrophage dataset.

606 Human Aging Lung

607 We downloaded the mammalian aging lung dataset by [Raredon et al.](#) from the Gene Expression  
608 Omnibus (accession number: [GSE133747](#)). The original dataset consists of human, pig, mouse and  
609 rat samples. We selected human samples and ran the preprocessing and quality control pipeline on  
610 them: normalization, log-transformation, selection of highly variable genes, batch-effect correction  
611 between donors using harmony ([Korsunsky et al., 2019](#)), computation of the nearest neighbor  
612 graph and Leiden clustering ([Traag et al., 2019](#)). The resulting dataset consisted of 17,867 cells  
613 from human male and female donors aged 21 to 88 years. We then projected the cell type labels  
614 from the human lung atlas onto the Raredon dataset by computing the DEGs between cell types in  
615 the Human lung atlas dataset and using the first 300 DEGs to identify equivalent cell types in the  
616 Raredon dataset and projecting those onto the Raredon dataset using the unsupervised cell type  
617 annotation tool scoreCT ([Seninge, 2020](#)). We identified 24 lung cell types from the HLCA. After using  
618 the cells from the 14 the human donors in the annotation step, we selected a set of 9 donors in order  
619 to obtain a balanced aging dataset, using the following inclusion criteria: 1) Donors contributing  
620 with very few cells were excluded (GSM4050113 and GSM4050107 consisted of 116 and 211 cells,  
621 respectively), 2) middle-aged donors were discarded in order to better explore the effects of aging,  
622 3) donors were selected to ensure sex-stratification, 4) we sought to obtain a balanced dataset in  
623 terms of age-group sizes. The final dataset consisted of 15,852 lung cells from 9 female and male  
624 human donors. We defined the age categories as young (21, 22, 32, 35 and 41 years old) and old  
625 (64, 65, 76 and 88 years old). The composition of the dataset was 7,263 young (46%) and 8,589 old  
626 cells (54%).

627 **Age-related change in transcriptional noise**

628 Measuring age-related loss of cell type membership

629 To facilitate comparison with regard to cell type annotation, we harmonized the labels so that the  
630 four datasets were annotated using the cell identities originally defined by [Angelidis et al.](#). Then,  
631 we measured transcriptional noise as 1 – membership to cell type clusters in the young and old  
632 fractions of each dataset. We then measured the age-related difference in transcriptional noise

633 per cell type by calculating the differences in median noise between the old and the young fraction  
634 for each lung cell type. In order to compare between the young and the old fraction of cells, each  
635 dataset was split into two datasets according to the age groups ("young" and "old"), and the highly  
636 variable gene detection and dimensionality reduction (PCA, batch-corrected neighbor detection  
637 using harmony, and UMAP) steps were run again on each set of cells. Then, *Scallop* was run on each  
638 set of cells separately, using Leiden as the community detection method and using the following  
639 parameter values: `frac_cells=0.8, n_trials=30`. This was done on a range of resolution (`res`)  
640 values between 0.1 and 1.5, with a step of 0.1, and the membership scores obtained for each cell  
641 were averaged over all these resolution values in order to smooth the effect of clustering granularity  
642 on the membership scores. We used the `freq` membership score, defined as the frequency of  
643 assignment of the most frequently assigned cluster label per cell.

#### 644 **Age-related cell type enrichment**

645 Changes in cell type abundance associated to aging were evaluated using binomial GLMs *McCullagh*  
646 and *Nelder* (1989). For each dataset, a binomial GLM was fitted to estimate the proportion of each  
647 cell type across all samples by treating each individual mouse as a replicate. First, the relative  
648 abundance of each cell type ( $N_{ct}$ ) and the relative abundance of the rest of the cell types taken  
649 together ( $N_{other}$ ) was computed. Then, a binomial GLM was fitted to these pairs of observations  
650 ( $N_{ct}, N_{other}$ ) to estimate the proportions of cell types across samples by accounting for variation  
651 associated to sample origin (mouse) and to sample age (young vs old), and estimated marginal  
652 means (Searle et al., 1980) were computed using the R package *emmeans*. Odds ratios between  
653 "Young" and "Old" samples were computed for each cell identity.

#### 654 **Data availability**

655 The Angelidis dataset was downloaded from the Gene Expression Omnibus (GSE124872). The  
656 original Kimmel dataset (consisting of kidney, spleen and lung samples) was downloaded from  
657 the Gene Expression Omnibus (GSE132901). The preprocessed and annotated files for the TMS  
658 datasets were downloaded from figshare (Pisco, 2020). The final version of the datasets as well as  
659 the reproducible Jupyter notebooks with all the analyses used in this study can be found in figshare  
660 (10.6084/m9.figshare.14981181).

#### 661 **Code availability**

662 The *Decibel* and *Scallop* repositories can be found at <https://gitlab.com/olgaibanez/decibel> and <https://gitlab.com/olgaibanez/scallop>, respectively. The reproducible Jupyter notebooks with the analyses  
663 carried out in this study can be found in figshare (10.6084/m9.figshare.14981181).

#### 665 **Funding**

666 This work was supported by grants from Instituto de Salud Carlos III (AC17/00012 and PI19/01621),  
667 cofunded by the European Union (European Regional Development Fund/ European Science Foun-  
668 dation, Investing in your future) and the 4D-HEALING project (ERA-Net program EracoSysMed, JTC-2  
669 2017); Diputación Foral de Gipuzkoa; Ministry of Science and Innovation of Spain; and PID2020-  
670 119715GB-I00 funded by MCIN/AEI/10.13039/501100011033 and by "ERDF A way of making Eu-  
671 rope". OI-S received the support of a fellowship from "la Caixa" Foundation (ID 100010434; code  
672 LCF/BQ/IN18/11660065), and from the European Union's Horizon 2020 research and innovation  
673 programme under the Marie Skłodowska-Curie grant agreement No. 713673. AMA was supported  
674 by a Basque Government Postgraduate Diploma fellowship (PRE\_2020\_2\_0081).

#### 675 **Acknowledgments**

676 We thank Iñaki Inza for his thorough revision of the manuscript, Laura Yndriago for her feedback,  
677 and Sandra Fuertes for useful discussions. We thank Valentine Svensson for support with the  
678 application of GLMs to cell type abundance analysis of scRNASeq data.

## 679 Author contributions

680 Conceptualization: OI-S; Funding Acquisition: MJA-B, OI-S, AMA; Investigation: OI-S, AMA, AI; Method-  
681 ology: OI-S, AMA; Project Administration: AI, MJA-B; Resources: MJA-B; Software: OI-S, AMA; Super-  
682 vision: AI; Visualization: OI-S, AMA; Writing - Original Draft Preparation: OI-S, AI; Writing - Review  
683 and Editing: OI-S, AMA, MJA-B, AI.

## 684 References

- 685 **Almanzar N, Antony J, the Tabula Muris Consortium.** A single-cell transcriptomic atlas characterizes ageing  
686 tissues in the mouse. *Nature*. 2020; doi: <https://doi.org/10.1038/s41586-020-2496-1>.
- 687 **Angelidis I, Simon LM, Fernandez IEea.** An atlas of the aging lung mapped by single cell transcriptomics and  
688 deep tissue proteomics. *Nature Communications*. 2019; doi: <https://doi.org/10.1038/s41467-019-08831-9>.
- 689 **Bacher R, Kendziora C.** Design and computational analysis of single-cell RNA-sequencing experiments. *Genome  
690 Biology*. 2016; 17:63. doi: <https://doi.org/10.1186/s13059-016-0927-y>.
- 691 **Bahar R, Hartmann CH, Rodriguez KA, Denny AD, Busuttil RA, Dollé MET, Calder RB, Chisholm GB, Pollock BH,  
692 Klein CA, et al.** Increased cell-to-cell variation in gene expression in ageing mouse heart. *Nature*. 2006;  
693 441(7096):1011–1014. doi: 10.1038/nature04844.
- 694 **Bezdek JC.** Pattern Recognition with Fuzzy Objective Function Algorithms. USA: Kluwer Academic Publishers;  
695 1981.
- 696 **Blondel VD, Guillaume JL, Lambiotte R, Lefebvre E.** Fast unfolding of communities in large networks. *Journal of  
697 Statistical Mechanics: Theory and Experiment*. 2008 oct; 2008(10):P10008. <https://doi.org/10.1088/1742-5468/2008/10/p10008>, doi: 10.1088/1742-5468/2008/10/p10008.
- 699 **Cagan A, Baez-Ortega A, Brzozowska N, Abascal F, Coorens THH, Sanders MA, Lawson ARJ, Harvey LMR, Bhosle  
700 S, Jones D, Alcantara RE, Butler TM, Hooks Y, Roberts K, Anderson E, Lunn S, Flach E, Spiro S, Januszczak I,  
701 Wrigglesworth E, et al.** Somatic mutation rates scale with lifespan across mammals. *Nature*. 2022; 604:517–524.  
702 doi: 10.1038/s41586-022-04618-z.
- 703 **Changyou S, Wang L, Sen P.** The eroding chromatin landscape of aging stem cells. *Translational Medicine of  
704 Aging*. 2020; 4:121–131. doi: [10.1016/j.tma.2020.08.002](https://doi.org/10.1016/j.tma.2020.08.002).
- 705 **Costa JPD, Vitorino R, Silva GM, Vogel C, Duarte AC, Rocha-Santos T.** A synopsis on aging—Theories, mechanisms  
706 and future prospects. *Ageing Research Reviews*. 2016; 29:90–112. doi: [10.1016/j.arr.2016.06.005](https://doi.org/10.1016/j.arr.2016.06.005).
- 707 **Dunn JC.** A Fuzzy Relative of the ISODATA Process and Its Use in Detecting Compact Well-Separated  
708 Clusters. *Journal of Cybernetics*. 1973; 3(3):32–57. <https://doi.org/10.1080/01969727308546046>, doi:  
709 10.1080/01969727308546046.
- 710 **Duò A RM, C S.** A systematic performance evaluation of clustering methods for single-cell RNA-seq data.  
711 *F1000Research*. 2018; 7(1141). doi: <https://doi.org/10.12688/f1000research.15666.2>.
- 712 **Enge M, Arda HE, Mignardi M, Beausang J, Bottino R, Kim SK, Quake SR.** Single-Cell Analysis of Human Pan-  
713 creas Reveals Transcriptional Signatures of Aging and Somatic Mutation Patterns. *Cell*. 2017; 171(2). doi:  
714 <https://doi.org/10.1016/j.cell.2017.09.004>.
- 715 **Fonseca Costa SS, Robinson-Rechavi M, Ripperger JA.** Single-cell transcriptomics allows novel insights into  
716 aging and circadian processes. *Brief Funct Genomics*. 2021; 19(5-6):343–349. doi: 10.1093/bfgp/ela014.
- 717 **Franceschi C, Bonafè M, Valensin S, Olivieri F, Luca MD, Ottaviani E, Benedictis GD.** Inflamm-aging: An Evolutionary  
718 Perspective on Immunosenescence. *Annals of the New York Academy of Sciences*. 2000; 908(1):244–254.  
719 doi: [10.1111/j.1749-6632.2000.tb06651.x](https://doi.org/10.1111/j.1749-6632.2000.tb06651.x).
- 720 **Frasca D, Blomberg BB.** Inflammaging decreases adaptive and innate immune responses in mice and humans.  
721 *Biogerontology*. 2015; 17(1):7–19. doi: 10.1007/s10522-015-9578-8.
- 722 **Freytag S, Tian L, Lönnstedt Iea.** Comparison of clustering tools in R for medium-sized 10x Genomics single-cell  
723 RNA-sequencing data. *F1000Research*. 2018; 7. doi: <https://doi.org/10.12688/f1000research.15809.1>.
- 724 **Gems D, de Magalhães JP.** The hoverfly and the wasp: A critique of the hallmarks of aging as a paradigm. *Ageing  
725 Res Rev*. 2021; 70(101407). doi: [10.1016/j.arr.2021.101407](https://doi.org/10.1016/j.arr.2021.101407).

- 726 **Gill D**, Parry A, Santos F, Okkenhaug H, Todd CD, Hernando-Herraez I, Stubbs TM, Milagre I, Reik W. Multi-omic  
727 rejuvenation of human cells by maturation phase transient reprogramming. *eLife*. 2022; 11(e71624). doi:  
728 [10.7554/elife.71624](https://doi.org/10.7554/elife.71624).
- 729 **Gladyshev VN**. Aging: progressive decline in fitness due to the rising deleteriome adjusted by genetic, environmental,  
730 and stochastic processes. *Aging Cell*. 2016; 15(4). doi: [10.1111/acel.12480](https://doi.org/10.1111/acel.12480).
- 731 **Goldfarbmuren KC**, Jackson ND, Sajuthi SP, Dyjack N, Li KS, Rios CL, Plender EG, Montgomery MT, Everman  
732 JL, Bratcher PE, et al. Dissecting the cellular specificity of smoking effects and reconstructing lineages in the  
733 human airway epithelium. *Nature Communications*. 2020; 11(1). doi: 10.1038/s41467-020-16239-z.
- 734 **Gupta K**, Yadav P, Maryam S, Ahuja G, Sengupta D. Quantification of age-related decline in transcriptional  
735 homeostasis. *J Mol Biol*. 2021; 433(19):167179. doi: [10.1016/j.jmb.2021.167179](https://doi.org/10.1016/j.jmb.2021.167179).
- 736 **Ham L**, Jackson M, Stumpf MP. Pathway dynamics can delineate the sources of transcriptional noise in gene  
737 expression. *eLife*. 2021; 10. doi: [10.7554/elife.69324](https://doi.org/10.7554/elife.69324).
- 738 **Hernando-Herraez I**, Evano B, Stubbs T, Commere PH, Bonder MJ, Clark S, Andrews S, Tajbakhsh S, Reik W.  
739 Ageing affects DNA methylation drift and transcriptional cell-to-cell variability in mouse muscle stem cells.  
740 *Nature Communications*. 2019; 10(1). doi: 10.1038/s41467-019-12293-4.
- 741 **Izgi H**, Han D, Isildak U, Huang S, Kocabiyik E, Khaitovich P, Somel M, Dönertas HM. Inter-tissue convergence of  
742 gene expression during ageing suggests age-related loss of tissue and cellular identity. *eLife*. 2022; 11. doi:  
743 [10.7554/elife.68048](https://doi.org/10.7554/elife.68048).
- 744 **Joost S**, Zeisel A, Jacob T, et al. Single-Cell Transcriptomics Reveals that Differentiation and Spatial Signatures  
745 Shape Epidermal and Hair Follicle Heterogeneity. *Cell Systems*. 2016; 3(3). doi: [doi:10.1016/j.cels.2016.08.010](https://doi.org/10.1016/j.cels.2016.08.010).
- 746 **Kimmel JC**, Penland L, Rubinstein ND, Hendrickson DG, Kelley DR, Rosenthal AZ. Murine single-cell RNA-seq  
747 reveals cell-identity- and tissue-specific trajectories of aging. *Genome Research*. 2019; 29(12):2088–2103. doi:  
748 [10.1101/gr.253880.119](https://doi.org/10.1101/gr.253880.119).
- 749 **Kirkwood TBL**, Melov S. On the Programmed/Non-Programmed Nature of Ageing within the Life History.  
750 *Current Biology*. 2011; 21(18). doi: [10.1016/j.cub.2011.07.020](https://doi.org/10.1016/j.cub.2011.07.020).
- 751 **Kiselev VY**, M ATSH. Challenges in unsupervised clustering of single-cell RNA-seq data. *Nature Reviews Genetics*.  
752 2019; 20. doi: <https://doi.org/10.1038/s41576-018-0088-9>.
- 753 **Korsunsky I**, Millard N, Fan J, Slowikowski K, Zhang F, Wei K, Baglaenko Y, Brenner M, Loh PR, Raychaudhuri  
754 S, et al. Fast, sensitive and accurate integration of single-cell data with Harmony. *Nature Methods*. 2019;  
755 16(12):1289–1296. doi: 10.1038/s41592-019-0619-0.
- 756 **Kovacs EJ**, Boe DM, Boule LA, Curtis BJ. Inflammaging and the lung. *Clinics in Geriatric Medicine*. 2017;  
757 33(4):459–471. doi: [10.1016/j.cger.2017.06.002](https://doi.org/10.1016/j.cger.2017.06.002).
- 758 **Levy O**, Amit G, Vaknin D, Snir T, Efroni S, Castaldi P, Liu YY, Cohen HY, Bashan A. Age-related loss of gene-  
759 to-gene transcriptional coordination among single cells. *Nature Metabolism*. 2020; 2(11):1305–1315. doi:  
760 10.1038/s42255-020-00304-4.
- 761 **Li J**, Zheng Y, Yan P, Song M, Wang S, Sun L, Liu Z, Ma S, Izpisua Belmonte JC, Chan P, Zhou Q, Zhang W, Liu  
762 GH, Tang F, Qu J. A single-cell transcriptomic atlas of primate pancreatic islet aging. *Natl Sci Rev*. 2020;  
763 8(2):nwaa127. doi: 10.1093/nsr/nwaa127.
- 764 **Lu Y**, Brommer B, Tian X, Krishnan A, Meer M, Wang C, Vera DL, Zeng Q, Yu D, Bonkowski MS, et al. Reprogramming  
765 to recover youthful epigenetic information and restore vision. *Nature*. 2020; 588(7836):124–129. doi:  
766 10.1038/s41586-020-2975-4.
- 767 **Lu Y**, Brommer B, Tian X, Krishnan A, Meer M, Wang C, Vera DL, Zeng Q, Yu D, Bonkowski MS, Yang JH, Zhou S,  
768 Hoffmann EM, Karg MM, Schultz MB, Kane AE, Davidsohn N, Korobkina E, Chwalek K, Rajman LA, et al. Reprogramming  
769 to recover youthful epigenetic information and restore vision. *Nature*. 2020; 588(7836):124–129.  
770 doi: 10.1038/s41586-020-2975-4.
- 771 **Lun A**, McCarthy D, Marioni J. A step-by-step workflow for low-level analysis of single-cell RNA-seq data with  
772 Bioconductor. *F1000Research*. 2016; 5(2122). doi: [10.12688/f1000research.9501.2](https://doi.org/10.12688/f1000research.9501.2).
- 773 **López-Otín C**, Blasco MA, Partridge L, Serrano M, Kroemer G. The Hallmarks of Aging. *Cell*. 2013;  
774 153(6):1194–1217. doi: [10.1016/j.cell.2013.05.039](https://doi.org/10.1016/j.cell.2013.05.039).

- 775 Ma S, Sun S, Geng L, Song M, Wang W, Ye Y, Ji Q, Zou Z, Wang S, He X, Li W, Rodriguez Esteban C, Long X, Guo G,  
776 Chan P, Zhou Q, Izpisua Belmonte JC, Zhang W, Qu J, Liu GH. Caloric restriction reprograms the single-cell tran-  
777 scriptional landscape of *Rattus Norvegicus* aging. *Cell*. 2020; 180:984–1001. doi: [10.1016/j.cell.2020.02.008](https://doi.org/10.1016/j.cell.2020.02.008).
- 778 Ma S, Sun S, Li J, Fan Y, Qu J, Sun L, Wang S, Zhang Y, Yang S, Liu Z, et al. Single-cell transcriptomic atlas of  
779 primate cardiopulmonary aging. *Cell Research*. 2020; 31(4):415–432. doi: [10.1038/s41422-020-00412-6](https://doi.org/10.1038/s41422-020-00412-6).
- 780 Martinez-Jimenez CP, Eling N, Chen HC, Vallejos CA, Kolodziejczyk AA, Connor F, Stojic L, Rayner TF, Stubbington  
781 MJT, Teichmann SA, de la Roche M, Marioni JC, T OD. Aging increases cell-to-cell transcriptional variability  
782 upon immune stimulation. *Science*. 2019; 20(366). doi: <https://doi.org/10.1126/science.aah4115>.
- 783 McCullagh P, Nelder JA. An outline of generalized linear models. *Generalized Linear Models*. 1989; p. 21–47.  
784 doi: [10.1007/978-1-4899-3242-6\\_2](https://doi.org/10.1007/978-1-4899-3242-6_2).
- 785 McInnes L, Healy J, Saul N, Großberger L. UMAP: Uniform manifold approximation and projection. *Journal of  
786 Open Source Software*. 2018; 3(29):861. doi: [10.21105/joss.00861](https://doi.org/10.21105/joss.00861).
- 787 McQuattie-Pimentel AC, Ren Z, Joshi N, Watanabe S, Stoeger T, Chi M, Lu Z, Sichizya L, Aillon RP, Chen CI, et al.  
788 The lung microenvironment shapes a dysfunctional response of alveolar macrophages in aging. *Journal of  
789 Clinical Investigation*. 2021; 131(4). doi: [10.1172/jci140299](https://doi.org/10.1172/jci140299).
- 790 Mendenhall AR, Martin GM, Kaeberlein M, Anderson RM. Cell-to-cell variation in gene expression and the aging  
791 process. *Geroscience*. 2021; 43(1):181–196. doi: [10.1007/s11357-021-00339-9](https://doi.org/10.1007/s11357-021-00339-9).
- 792 Misharin AV, Morales-Nebreda L, Reyfman PA, Cuda CM, Walter JM, McQuattie-Pimentel AC, Chen CI, Anekalla KR,  
793 Joshi N, Williams KJN, et al. Monocyte-derived alveolar macrophages drive lung fibrosis and persist in the lung  
794 over the life span. *Journal of Experimental Medicine*. 2017; 214(8):2387–2404. doi: [10.1084/jem.20162152](https://doi.org/10.1084/jem.20162152).
- 795 Mishra S, Srivastava D, Kumar V. Improving gene network inference with graph wavelets and making in-  
796 sights about ageing-associated regulatory changes in lungs. *Brief Bioinform*. 2021; 22(4):bbaa360. doi:  
797 [10.1093/bib/bbaa360](https://doi.org/10.1093/bib/bbaa360).
- 798 Moignard V, Woodhouse S, Haghverdi L, et al. Decoding the regulatory network of early blood development from  
799 single-cell gene expression measurements. *Nature Biotechnology*. 2015; 33(3). doi: [doi:10.1038/nbt.3154](https://doi.org/10.1038/nbt.3154).
- 800 Munkres J. Algorithms for the Assignment and Transportation Problems. *Journal of the Society of Industrial  
801 and Applied Mathematics*. 1957; 5(1).
- 802 Nalapareddy K, Zheng Y, Geiger H. Aging of intestinal stem cells. *Stem Cell Reports*. 2022; 17(4):734–740. doi:  
803 [10.1016/j.stemcr.2022.02.003](https://doi.org/10.1016/j.stemcr.2022.02.003).
- 804 Nikopoulou C, Parekh S, Tessarz P. Ageing and sources of transcriptional heterogeneity. *Biological Chemistry*.  
805 2019; 400(7):867–878. doi: [10.1515/hsz-2018-0449](https://doi.org/10.1515/hsz-2018-0449).
- 806 Oh J, Lee YD, Wagers AJ. Stem cell aging: Mechanisms, regulators and therapeutic opportunities. *Nature  
807 Medicine*. 2014; 20(8):870–880. doi: [10.1038/nm.3651](https://doi.org/10.1038/nm.3651).
- 808 Olah M, Patrick E, Villani AC, Xu J, White CC, Ryan KJ, Piehowski P, Kapasi A, Nejad P, Cimpean M, et al. A  
809 transcriptomic atlas of aged human microglia. *Nature Communications*. 2018; 9(1). doi: [10.1038/s41467-018-02926-5](https://doi.org/10.1038/s41467-018-02926-5).
- 810 Oliviero G, Kovalchuk S, Rogowska-Wrzesinska A, Schwämmle V, Jensen ON. Distinct and diverse chromatin  
811 proteomes of ageing mouse organs reveal protein signatures that correlate with physiological functions. *eLife*.  
812 2022; 11(e73524). doi: [10.7554/eLife.73524](https://doi.org/10.7554/eLife.73524).
- 813 Park JE, K P, K M, Teichmann SA. Fast Batch Alignment of Single Cell Transcriptomes Unifies Multiple Mouse  
814 Cell Atlases into an Integrated Landscape. *bioRxiv*. 2018; <https://www.biorxiv.org/content/early/2018/08/22/397042>, doi: [10.1101/397042](https://doi.org/10.1101/397042).
- 815 Paul F, Arkin Y, Giladi A, et al. Transcriptional Heterogeneity and Lineage Commitment in Myeloid Progenitors.  
816 *Nature Biotechnology*. 2015; 163(7). doi: [doi:10.1016/j.cell.2015.11.013](https://doi.org/10.1016/j.cell.2015.11.013).
- 817 Pawelec G. Hallmarks of human “immunosenescence”: adaptation or dysregulation? *Immunity & ageing*. 2012;  
818 9(1). doi: [doi.org/10.1186/1742-4933-9-15](https://doi.org/10.1186/1742-4933-9-15).
- 819 Pisco A. Tabula muris senis. Processed files (to use with scanpy). . 2020; doi: [10.6084/m9.figshare.12654728.v1](https://doi.org/10.6084/m9.figshare.12654728.v1).

- 822 Pálovics R, Keller A, Schaum N, Tan W, Fehlmann T, Borja M, Kern F, Bonanno L, Calcuttawala K, Webber J,  
823 McGeever A, Consortium TTM, Luo J, Pisco AO, Karkanias J, Neff NF, Darmanis S, Quake SR, Wyss-Coray T.  
824 Molecular hallmarks of heterochronic parabiosis at single-cell resolution. *Nature*. 2022; 603:309–314. doi:  
825 10.1038/s41586-022-04461-2.
- 826 Raredon MSB, Adams TS, Suhail Y, Schupp JC, Poli S, Neumark N, Leiby KL, Greaney AM, Yuan Y, Horien C,  
827 et al. Single-cell connectomic analysis of adult mammalian lungs. *Science Advances*. 2019; 5(12). doi:  
828 10.1126/sciadv.aaw3851.
- 829 Raser JM, O’Shea EK. Noise in gene expression: origins, consequences, and control. *Science*. 2005;  
830 309(5743):2010–2013. doi: 10.1126/science.1105891.
- 831 Rhoades NS, Davies M, Lewis SA, Cinco IR, Kohama SG, Bermudez LE, Winthrop KL, Fuss C, Mattison JA, Spindel  
832 ER, Messaoudi I. Functional, transcriptional, and microbial shifts associated with healthy pulmonary aging in  
833 rhesus macaques. *Cell Reports*. 2022; 39(110725). doi: 10.1016/j.celrep.2022.110725.
- 834 Salminen A. Feed-forward regulation between cellular senescence and immunosuppression promotes the  
835 aging process and age-related diseases. *Ageing Res Rev*. 2021; 67(101280). doi: 10.1016/j.arr.2021.101280.
- 836 Salzer MC, Lafzi A, Berenguer-Llergo A, Youssif C, Castellanos A, Solanas G, Peixoto FO, Attolini CSO, Prats N,  
837 Aguilera M, et al. Identity Noise and Adipogenic Traits Characterize Dermal Fibroblast Aging. *Cell*. 2018; 175(6).  
838 doi: 10.1016/j.cell.2018.10.012.
- 839 Satija R, Farrell DJ, Gennert J, Schier AF, Regev A. Spatial reconstruction of single-cell gene expression data.  
840 *Nature Biotechnology*. 2015; doi: <https://doi.org/10.1038/nbt.3192>.
- 841 Schaum N, Lehallier B, Hahn O, Pálovics R, Hosseinzadeh S, Lee SE, Sit R, Lee DP, Morán Losada P, Zardeneta  
842 ME, Fehlmann T, Webber JT, McGeever A, Calcuttawala K, Zhang H, Berdnik D, Mathur V, Tan W, Zee A, Tan  
843 M, et al. Ageing hallmarks exhibit organ-specific temporal signatures. *Nature*. 2020; 583:309–314. doi:  
844 10.1038/s41586-022-04461-2.
- 845 Schiller HB, Montoro DT, Simon LM, Rawlins EL, Meyer KB, Strunz M, Vieira Braga FA, Timens W, Koppelman  
846 GH, Budinger GR, et al. The Human Lung Cell Atlas: A high-resolution reference map of the human lung  
847 in health and disease. *American Journal of Respiratory Cell and Molecular Biology*. 2019; 61(1):31–41. doi:  
848 10.1165/rccm.2018-0416tr.
- 849 Schmeier C, Kretz A, Wengerdt D, Stojiljkovic MA, Witte OW. Dissecting Aging and Senescence-Current Concepts  
850 and Open Lessons. *Cells*. 2019; 8(11). doi: doi:10.3390/cells8111446.
- 851 Schneider JL, Rowe JH, Garcia-de Alba C, Kim CF, Sharpe AH, Haigis MC. The aging lung: Physiology, disease,  
852 and immunity. *Cell*. 2021; 184(8):1990–2019. doi: 10.1016/j.cell.2021.03.005.
- 853 Searle SR, Speed FM, Milliken GA. Population Marginal Means in the Linear Model: An Alternative to Least  
854 Squares Means. *The American Statistician*. 1980; 34(4):216–221. doi: 10.1080/00031305.1980.10483031.
- 855 Seninge L. scoreCT: Automated Cell Type Annotation. GitHub repository. 2020; .
- 856 Sikkema L, Strobl D, Zappia L, Madisoone E, Markov NS, Zaragoza L, Ansari M, Arguel M, Apperloo L, Bé-  
857 cavín C, Berg M, Chichelnitskiy E, Chung M, Collin A, Gay ACA, Hooshiar Kashani B, Jain M, Kapellos T, Kole  
858 TM, Mayr C, et al. An integrated cell atlas of the human lung in health and disease. *bioRxiv*. 2022; doi:  
859 10.1101/2022.03.10.483747.
- 860 Solé-Boldo L, Raddatz G, Schütz Sea. Single-cell transcriptomes of the human skin reveal age-related loss of  
861 fibroblast priming. *Commun Biol*. 2020; 3(188). doi: <https://doi.org/10.1038/s42003-020-0922-4>.
- 862 Takemoto Y, Chick JM, Gerdes Gyuricza I, Skelly DA, Devuyst O, Gygi SP, Churchill GA, Korstanje R. Proteomic and  
863 transcriptomic profiling reveal different aspects of aging in the kidney. *eLife*. 2021; 10. doi: 10.7554/elife.62585.
- 864 Tasic B, Menon V, Nguyen TN, Kim TK, Jarsky T, Yao Z, Levi B, Gray LT, Sorensen SA, Dolbeare T, et al. Adult mouse  
865 cortical cell taxonomy revealed by single cell transcriptomics. *Nature Neuroscience*. 2016; 19(2):335–346. doi:  
866 10.1038/nn.4216.
- 867 Traag VA, Waltman L, van Eck NJ. From Louvain to Leiden: guaranteeing well-connected communities. *Scientific  
868 Reports*. 2019; 9. doi: <https://doi.org/10.1038/s41598-019-41695-z>.
- 869 Trapnell C. Defining cell types and states with single-cell genomics. *Genome Research*. 2015; 25(10):1491–1498.  
870 doi: 10.1101/gr.190595.115.

- 871 **Travaglini KJ**, Nabhan AN, Penland L, Sinha R, Gillich A, Sit RV, Chang S, Conley SD, Mori Y, Seita J, et al. A  
872 molecular cell atlas of the human lung from single-cell RNA sequencing. *Nature*. 2020; 587(7835):619–625.  
873 doi: 10.1038/s41586-020-2922-4.
- 874 **Uyar B**, Palmer D, Kowald A, Murua-Escobar H, Barrantes I, Möller S, Akalin A, Fuellen G. Single-  
875 cell analyses of aging, inflammation and senescence. *Ageing Res Rev*. 2020; 64(101156). doi:  
876 <https://doi:10.1016/j.arr.2020.101156>.
- 877 **Vijg J**. From DNA damage to mutations: All roads lead to aging. *Ageing Res Rev*. 2021; 68(101316). doi:  
878 <https://doi:10.1016/j.arr.2021.101316>.
- 879 **Waltman L**, van Eck NJ, Traag VA. A smart local moving algorithm for large-scale modularity-based community  
880 detection. *European Physical Journal B*. 2013; 86.
- 881 **Warren LA**, Rossi DJ, Schiebinger GR, Weissman IL, Kim SK, Quake SR. Transcriptional instability is not a universal  
882 attribute of aging. *Aging Cell*. 2007; 6(6):775–782. doi: [10.1111/j.1474-9726.2007.00337.x](https://doi:10.1111/j.1474-9726.2007.00337.x).
- 883 **Williamson EJ**, Walker AJ, Bhaskaran K, Bacon S, Bates C, Morton CE, Curtis HJ, Mehrkar A, Evans D, Inglesby P,  
884 et al. Factors associated with COVID-19-related death using OpenSAFELY. *Nature*. 2020; 584(7821):430–436.  
885 doi: 10.1038/s41586-020-2521-4.
- 886 **Wolf FA**, P A, Theis FJ. SCANPY: large-scale single-cell gene expression data analysis. *Genome Biology*. 2018; doi:  
887 <https://doi.org/10.1186/s13059-017-1382-0>.
- 888 **Ximerakis M**, Lipnick SL, Innes BT, Simmons SK, Adiconis X, Dionne D, Mayweather BA, Nguyen L, Niziolak Z, Ozek  
889 C, Butty VL, Isserlin R, Buchanan SM, Levine SS, Regev A, Bader GD, Levin JZ, Rubin LL. Single-cell transcriptomic  
890 profiling of the aging mouse brain. *Nat Neurosci*. 2019; 22(10). doi: <https://doi:10.1038/s41593-019-0491-3>.
- 891 **Yang JH**, Griffin PT, Vera DL, Apostolides JK, Hayano M, Meer MV, Salfati EL, Su Q, Munding EM, Blanchette M,  
892 Bhakta M, Dou Z, Xu C, Pippin JW, Creswell ML, O'Connell BL, Green RE, Garcia BA, Berger SL, Oberdoerffer  
893 P, et al. Erosion of the Epigenetic Landscape and Loss of Cellular Identity as a Cause of Aging in Mammals.  
894 bioRxiv. 2019; <https://www.biorxiv.org/content/early/2019/10/19/808642>, doi: 10.1101/808642.
- 895 **Yousefzadeh MJ**, Flores RR, Zhu Y, Schmiechen ZC, Brooks RW, Trussoni CE, Cui Y, Angelini L, Lee KA, McGowan  
896 SJ, Burrack AL, Wang D, Dong Q, Lu A, Sano T, O'Kelly R, McGuckian CA, Kato JI, Bank MP, Wade EA, et al. An  
897 aged immune system drives senescence and ageing of solid organs. *Nature*. 2021; 594(7861):100–105. doi:  
898 10.1038/s41586-021-03547-7.
- 899 **Zhang W**, Zhang S, Yan P, Ren J, Song M, Li J, Lei J, Pan H, Wang S, Ma X, et al. A single-cell transcriptomic  
900 landscape of primate arterial aging. *Nature Communications*. 2020; 11(1). doi: 10.1038/s41467-020-15997-0.
- 901 **Zhu L**, Lei J, Klei L, Devlin B, Roeder K. Semisoft clustering of single-cell data. *Proceedings of the National Academy  
902 of Sciences*. 2019; 116(2):466–471. <https://www.pnas.org/content/116/2/466>, doi: [10.1073/pnas.1817715116](https://doi:10.1073/pnas.1817715116).
- 903 **Zou Z**, Long X, Zhao Q, Zheng Y, Song M, Ma S, Jing Y, Wang S, He Y, Esteban CR, et al. A Single-Cell Transcriptomic  
904 Atlas of Human Skin Aging. *Developmental Cell*. 2021; 56(3). doi: [10.1016/j.devcel.2020.11.002](https://doi:10.1016/j.devcel.2020.11.002).
- 905

## Appendix 1

906

Dataset	n_cells	n_genes	median_genes_per_cell	n_populations
PBMC3K	2700	32738	817	12
Joost <i>et al.</i>	1422	6410	1941	17
Paul <i>et al.</i>	2730	3451	872	14
Moignard <i>et al.</i>	3934	42	42	9
Heart10K	7713	11765	2035	26

907  
908 **Appendix 1 Table 1. Datasets used in the technical validation of *Scallop*.** Number of cells, number of genes, median number of genes  
909 per cell and number of estimated cell populations in each dataset.  
910

911

## Appendix 2

912

Dataset	Tissue	Organism	N. cells	Noise	Scope	Method
<i>Enge et al.</i>	Pancreas	Human	2,544	Yes	In Beta cells.	1) Biological over technical variation, 2) whole transcriptome-based Euclidean distance to cell type mean, 3) invariant gene-based Euclidean distance to cell type mean.
<i>Martinez-Jimenez et al.</i>	CD4+ T cells	Mouse	1,513	Yes	Single cell type studied.	Percentage of cells expressing the core activation program.
<i>Angelidis et al.</i>	Lung	Mouse	14,813	Yes	In most cell types.	Distance to cell type mean.
<i>Kimmel et al.</i>	Lung, spleen, kidney	Mouse	30,255 30,512 29,815	Yes	In many cell types.	1) Overdispersion of genes, 2) invariant gene-based Euclidean distance to cell type mean, 3) whole transcriptome-based Manhattan distance to cell type mean.
<i>Ximerakis et al.</i>	Brain	Mouse	37,069	No	Differences in magnitude and directionality between cell types.	Coefficient of variation of 1) all genes, 2) mitochondrial genes, 3) ribosomal genes.
<i>Salzer et al.</i>	Dermal fibroblasts	Mouse	731	Yes	Single cell type studied.	Compactness of clusters on PCA plot.
<i>Solé-Boldo et al.</i>	Skin	Human	22,142	Yes	In dermal fibroblasts.	Less clear GO annotations.

913  
914  
915  
916  
917  
918  
919  
920  
**Appendix 2 Table 1.** Seven scRNAseq studies of different tissues where age-related increase in transcriptional noise was measured. The number of cells (*N. cells*) in the table is the size of the dataset prior to quality control. The *Noise* column states whether an increase in transcriptional noise was reported in some/all cell types in the original articles. The *Scope* column summarizes the cell types where age-related increase in transcriptional noise was reported. The *Method* column specifies how transcriptional noise was measured in the original articles.

## Appendix 3

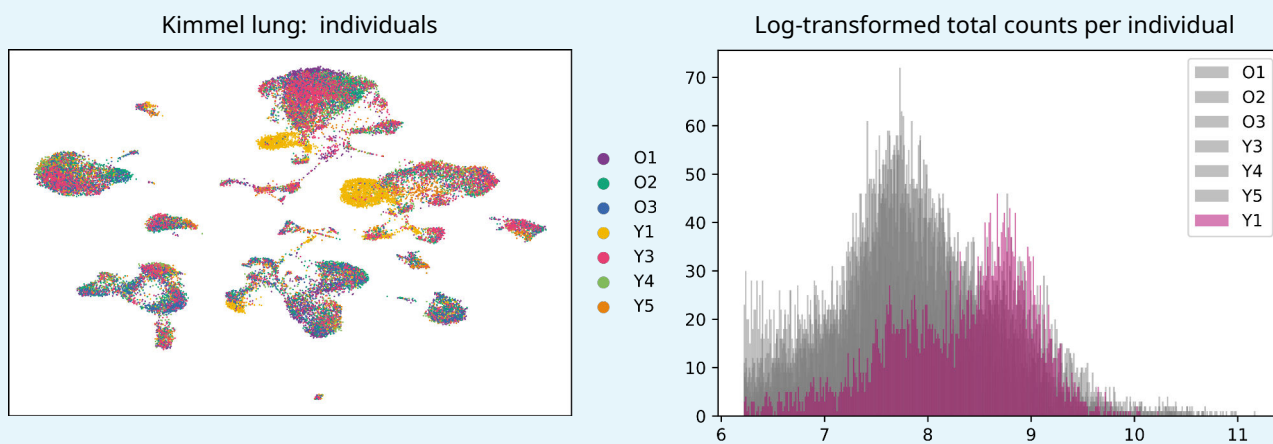
921

Dataset	Inclusion criteria	Number of individuals	Number of cells	Ages
<i>Enge et al.</i>	All samples except those from pediatric individuals (0-6 y old)	Young: 2 Old: 3	Young: 791 Old: 1,023	Young: 21 and 22 y Old: 38, 44 and 58 y
<i>Martinez-Jimenez et al.</i>	Whole dataset.	Young: 9 Old: 12	Young: 532 Old: 981	Young: 3 m Old: 24 mo
<i>Angelidis et al.</i>	Whole dataset.	Young: 8 Old: 7	Young: 7,644 Old: 6,526	Young: 3 m Old: 24 m
<i>Kimmel et al.</i>	Lung samples from all mice except Y1.	Young: 3 Old: 3	Young: 13,352 Old: 12,998	Young: 7 m Old: 24 m
<i>Ximerakis et al.</i>	Whole dataset.	Young: 8 Old: 8	Young: 16,028 Old: 21,041	Young: 2-3 m Old: 21-23 m
<i>Salzer et al.</i>	All samples except those from newborn mice.	Young: 4 Old: 4	Young: 329 Old: 332	Young: 2 m Old: 18 m
<i>Solé-Boldo et al.</i>	Whole dataset.	Young: 2 Old: 3	Young: 8,316 Old: 13,826	Young: 25 and 27 y Old: 53, 69 and 70 y

922  
923 **Appendix 3 Table 1.** The general criteria for inclusion in the aging datasets used in this study was to include all samples from young and  
924 old individuals and to exclude newborn or pediatric individuals, as we did for the human pancreatic cell dataset (*Enge et al., 2017*) and the  
925 murine dermal fibroblast dataset (*Salzer et al., 2018*). Care was taken to make all aging datasets sex-balanced. This was not possible for  
926 some datasets, as they consisted of same-sex individuals. However, same-sex datasets were included in our study as sex could not be a  
927 confounding factor in the aging analysis.  
928

## Appendix 4

929

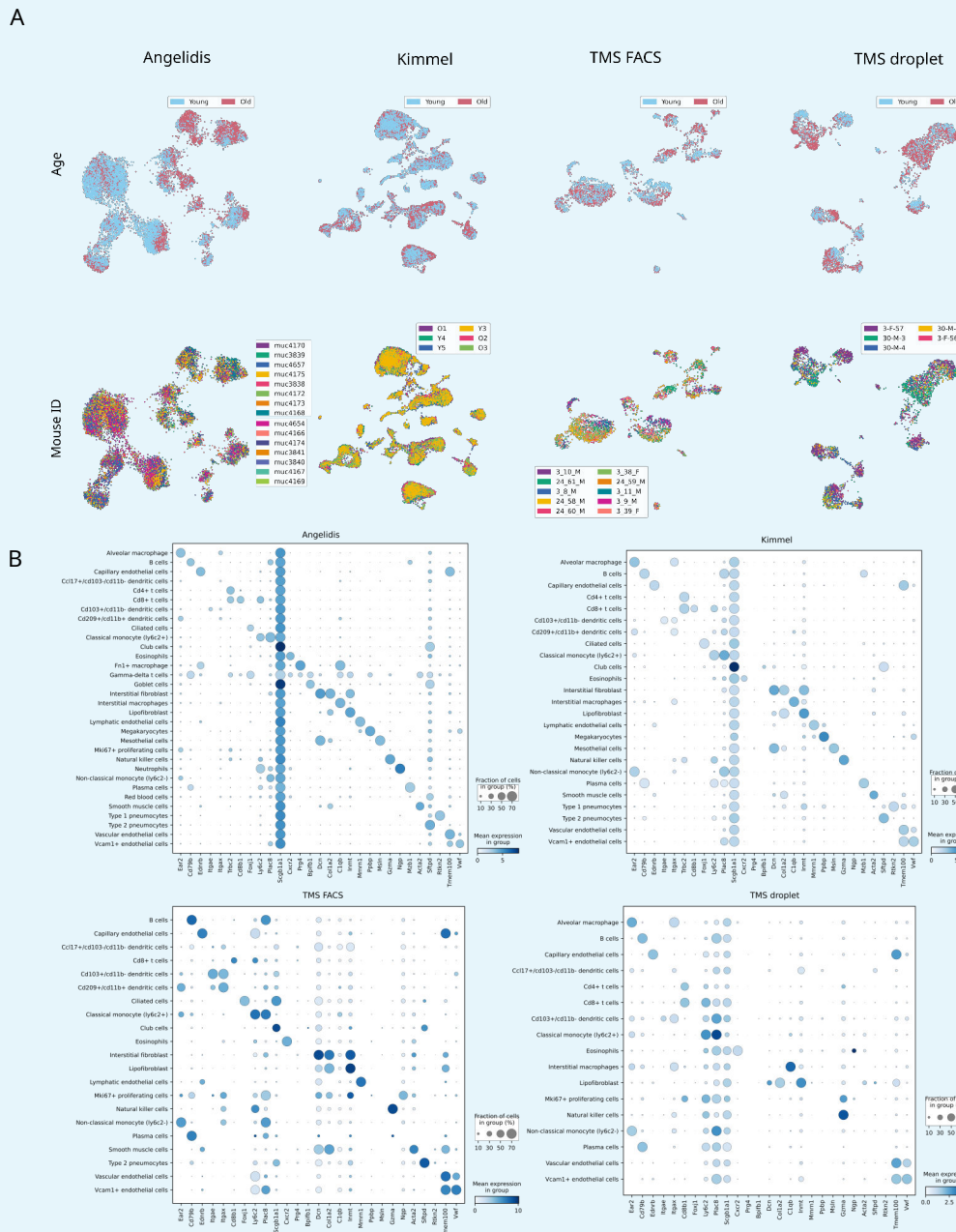


930  
931  
932  
933  
934  
935  
936  
937  
938

**Appendix 4 Figure 1. UMAP plot showing the samples from the seven individuals present in the Kimmel lung dataset.** Even though most cells cluster together according to their cell type rather than by individual, samples from donor Y1 cluster together. We observed that there was a big batch effect between this and the rest of the individuals. **Histogram showing the log-transformed total number of counts/cell per individual mice.** The distribution of counts/cell of the samples from mouse Y1 is very different to the rest of the samples. This difference could not be overcome using the batch-effect correction tool *bbknn*. Downsampling the counts so that the number of counts/cell was balanced across individual mice did not solve the problem either. Therefore, we decided to discard the samples Y1L1 and Y1L2.

## Appendix 5

939



**Appendix 5 Figure 1. (A) There are no mouse- or age-related batch effects.** UMAP plots of the four aging lung datasets showing the age and mouse labels. Cells cluster according to their cell type rather than to their age group or individual mouse. **(B) Expression of lung cell type markers by each annotated cluster.** The dotplots show the expression of the cell type markers from *Angelidis et al.* on the four annotated lung datasets. The size of the dots represents the fraction of cells expressing one particular marker in the group of cells assigned a particular cell type label. The color represents the level of expression of the marker in that group averaged over the cells that have a positive expression of that marker.

940

941

942

943

940

245

943

94

## Appendix 6

948

949  
950

Dataset	N. young cells	N. old cells	N. young donors	N. old donors	Total cells
<i>Raredon et al.</i>	7,263	8,589	3 females: 21, 32, 41 years old 2 males: 22, 35 years old	2 females: 76, 88 years old 2 males: 64, 65 years old	15,852
<i>Travaglini et al. (HLCA)</i>	7,524	7,524	1 male: 46 years old	1 male: 75 years old	15,048

952  
**Appendix 6 Table 1.** Number of cells, sex and age composition of the human aging lung datasets.

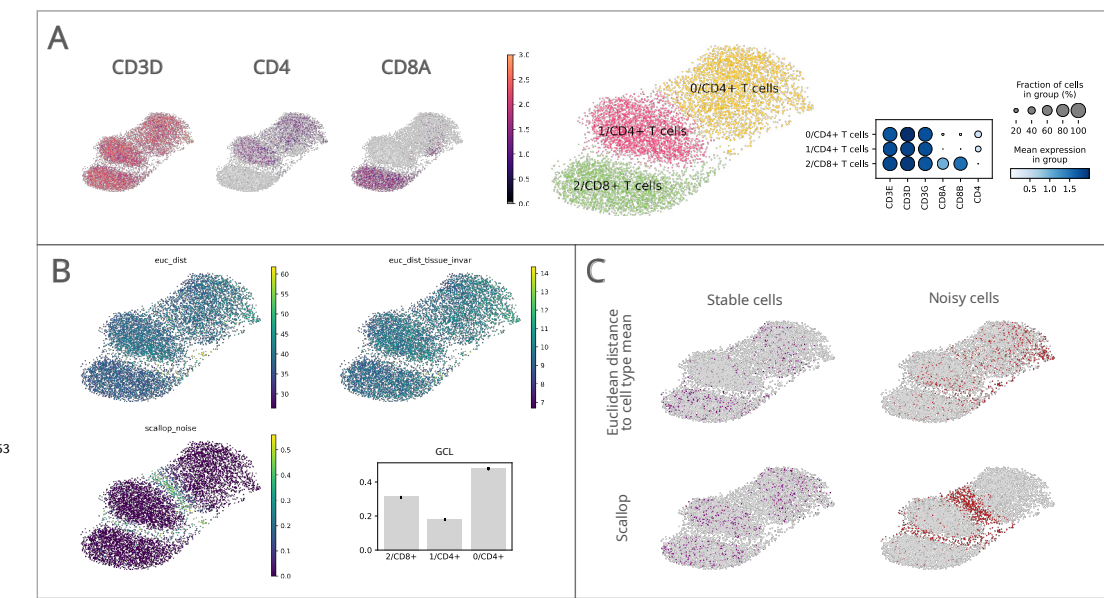


**Figure 1-Figure supplement 1. Performance of Scallop in comparison to preexisting methods for the quantification of transcriptional noise.** The different methods were tested on a dataset of 8,278 human T lymphocytes. (A) UMAPs and dotplot showing *CD3*, *CD4* and *CD8* marker gene expression per cluster. (B) Representation of transcriptional noise levels, as measured by using two distance-to-centroid methods (*euc\_dist* and *euc\_dist\_tissue\_invar*), 1 – membership (*scallop\_noise*) and Global Coordination Level (*GCL*). (C) The 10% most stable (purple) and 10% most unstable (red) cells are represented on the UMAP plots for *Euclidean distance to cell type mean* (top row) and *Scallop* methods (bottom row), respectively.

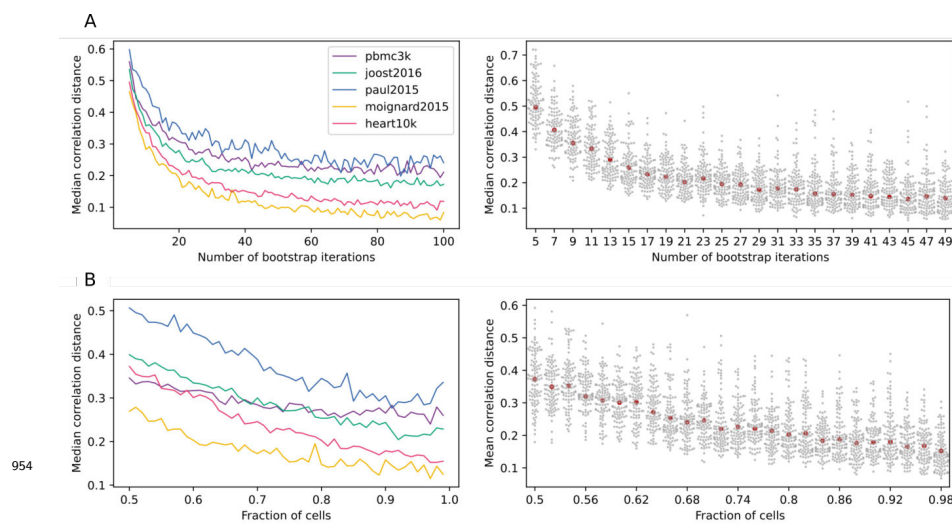


**Figure 1–Figure supplement 2. *Scallop* robustness in relation to input parameters.** The plots on the left show the median correlation distance between membership scores of different runs of *Scallop* against (A) the number of trials, (B) the fraction of cells used in each bootstrap and (C) the resolution given to the clustering method (Leiden) in five independent scRNAseq datasets (**PBMC3K**, **Joost et al. (2016)**; **Paul et al. (2015)**; **Moignard et al. (2015)**, **Heart10k**). The median correlation distance was computed over 100 runs of *Scallop*. The swarmplots on the right show the distribution of the correlation distances between membership scores against each of the input parameters for the heart10k dataset. The median is shown as a red point. While, for the sake of clarity, a random sample of 100 correlation distances is shown for each value of the parameter under study, the median was computed using all the correlation distances. *Scallop* membership scores converge as we increase the number of bootstrap iterations and the fraction of cells used in the clustering.

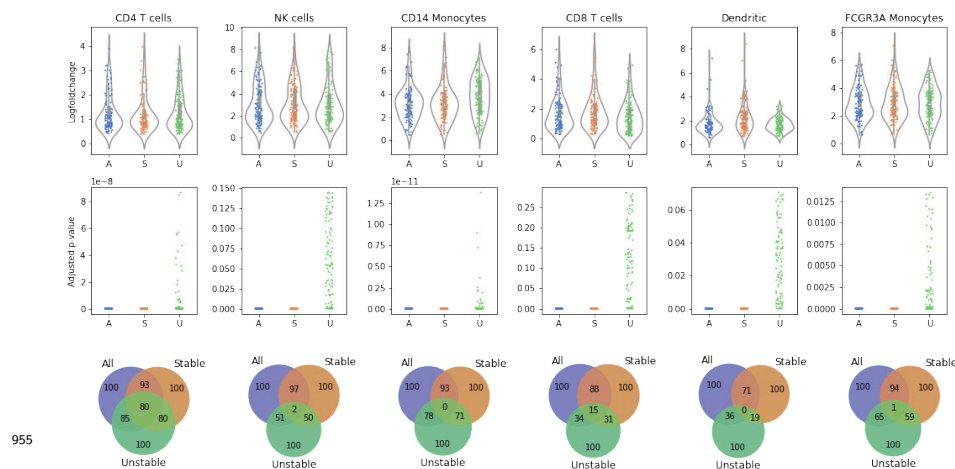


**Figure 1-Figure supplement 3. Stable cells as identified with *Scallop* are more representative of the cell type than unstable cells.** Distribution of log-fold changes (top row) and adjusted *p*-values (middle row) of the first 100 differentially expressed genes (DEGs) between each cell type or subtype and the rest of the cells in six cell types and subtypes from the 10X PBMC3K dataset. The overlap between the DEGs found when using all of the cells, only the stable cells and only the unstable cells is also shown (bottom row). The adjusted *p*-values obtained with all the cells are equivalent to those obtained using only the most stable half of the cells. In contrast, the differential expression of many genes is not statistically significant when using the unstable half from each population. The overlap between the top 100 DEGs obtained is very high between the stable cells and all cells subsets, whereas DEGs obtained in unstable cells have a very low intersection with all cells.

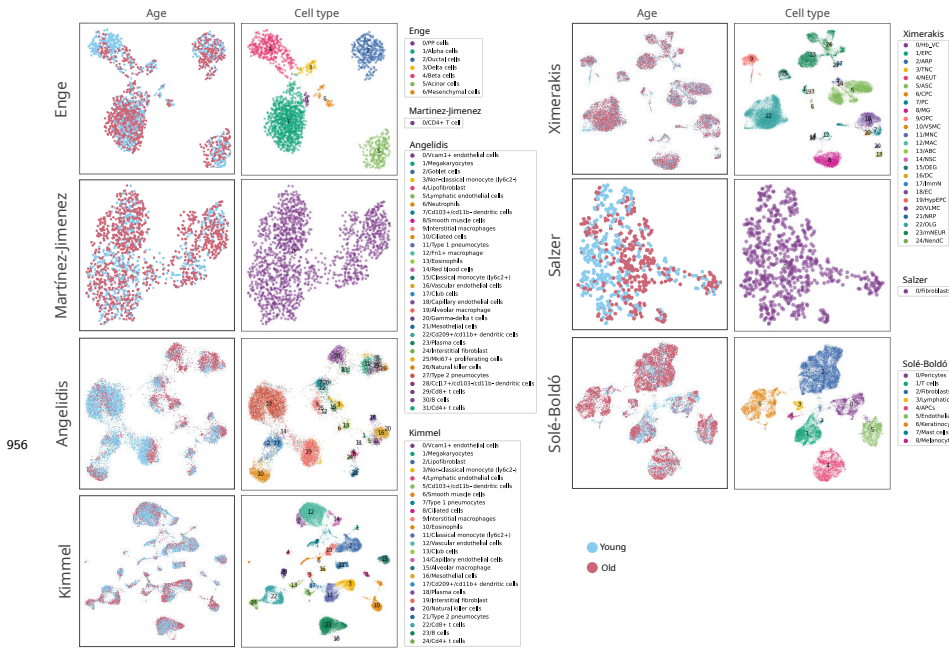


**Figure 2-Figure supplement 1. Composition of the seven scRNAseq datasets of aging used in this figure.** UMAPs showing the age and cell type composition of the seven datasets used in the analysis of the age-related transcriptional noise at the tissue level. The UMAPs show the final composition of the datasets used in the experiment. The cell type annotations were obtained from the original authors in all datasets except Kimmel lung, where the labels from Angelidis were projected onto the dataset.

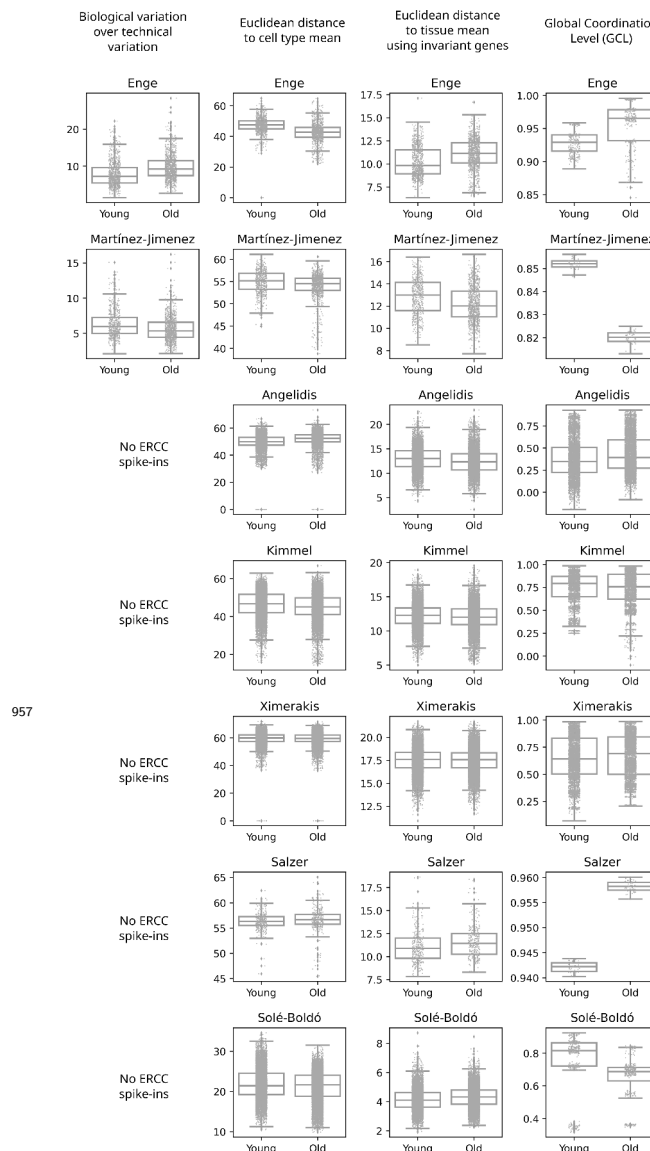


**Figure 2-Figure supplement 2. Measurements of transcriptional noise on seven scRNAseq datasets of aging using computational methods implemented in *Decibel*.** Stripplots showing the distribution of noise values, as measured by the four alternative methods (Biological variation over technical variation, Euclidean distance to cell type mean, Euclidean distance to tissue mean using invariant genes, and Global Coordination Level - GCL) in the seven datasets used in the analysis of the age-related transcriptional noise at the tissue level. Boxplots and their whiskers represent the interquartile range (IR) and 1.5\*IR respectively.

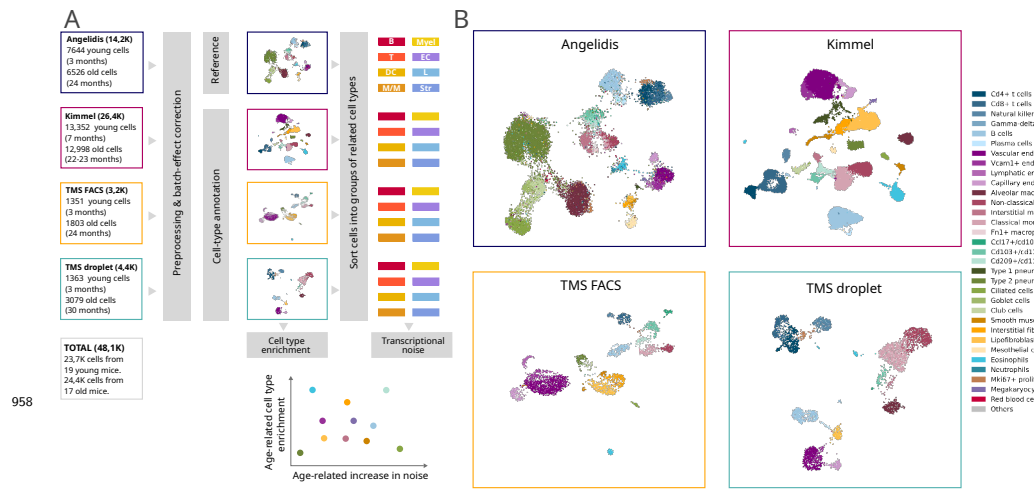


**Figure 3-Figure supplement 1. Composition of the four scRNAseq datasets of the murine aging lung used in this figure.** (a) Experimental approach. Four murine aging lung datasets were preprocessed and cell type-annotated. The cell-type labels from Angelidis were used as a reference to annotate the rest of the datasets. Differences in cell-type abundance between young and old mice were quantified using GLMs. From each dataset, eight subsets of related cell-types were created to classify the 31 cell types into 8 categories, which were used as input for *Scallop* to analyze the differences in cell-to-cell variability. (b) Cell type-annotated mouse lung datasets. UMAP plots showing the four datasets with their cell type annotations.

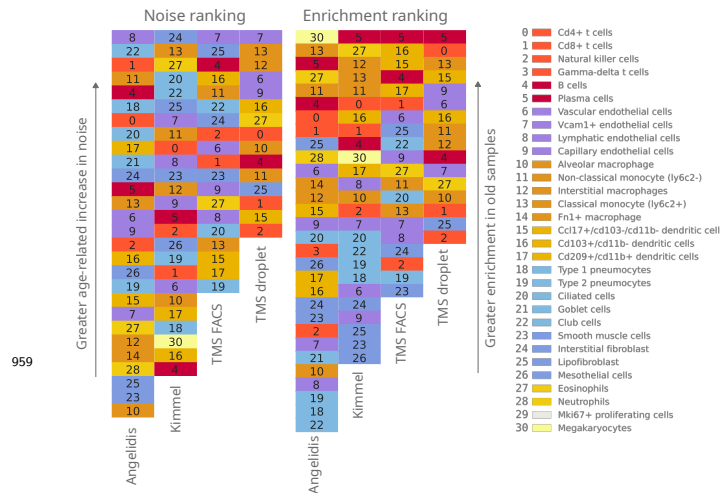


**Figure 3-Figure supplement 2. Qualitative ranking of murine aging lung cell types according to transcriptional noise and cell type enrichment.** The 31 detected lung cell types were classified in the *Noise* ranking (left) according to their greater age-related increase in noise. They were also classified in the *Enrichment* ranking (right) according to their greater enrichment in old samples. Cell categories that were represented by fewer than 100 cells were excluded from the transcriptional noise evaluation, and therefore do not appear in the plot. Specific cell types are shown in the same color and with the same numbers as specified in the legend.

960

	Angelidis_TN	Kimmel_OD	Kimmel_DC	Angelidis_S	Kimmel_S	TMS_FACS_S	TMS_drop_S
Cd4+ t cells	UP	DOWN	UP	UP	UP	NP	NS
Cd8+ t cells	NS	DOWN	UP	UP	NS	UP	DOWN
Natural killer cells	NS	NS	UP	DOWN	NS	NS	DOWN
Gamma-delta t cells	NS	NP	NP	NP	DOWN	NP	NP
B cells	UP	DOWN	UP	UP	DOWN	UP	DOWN
Plasma cells	NS	NP	NP	NS	NS	NS	NS
Alveolar macrophage	UP	UP	DOWN	DOWN	DOWN	NP	NS
Non-classical monocyte (ly6c2-)	UP	DOWN	UP	UP	UP	UP	DOWN
Interstitial macrophages	NS	NP	NP	DOWN	NS	NP	NS
Classical monocyte (ly6c2+)	NS	UP	UP	NS	UP	NS	NS
Fn1+ macrophage	UP	NP	NP	DOWN	NP	NP	NP
Ccl17+/cd103-/cd11b- dendritic cells	NS	NP	NS	NS	NS	NS	NS
Cd103+/cd11b- dendritic cells	UP	NP	NP	DOWN	UP	NP	NS
Cd209+/cd11b+ dendritic cells	UP	NP	NP	UP	NS	DOWN	NP
Eosinophils	NS	NP	NP	NP	UP	NS	DOWN
Neutrophils	UP	NP	NP	DOWN	NP	NP	NP
Megakaryocytes	NS	NP	NP	NP	UP	NP	NP
Vascular endothelial cells	UP	NP	NP	UP	DOWN	UP	UP
Vcam1+ endothelial cells	UP	NP	NP	NS	NS	UP	UP
Lymphatic endothelial cells	NS	NP	NP	UP	UP	UP	NP
Capillary endothelial cells	NS	NP	NP	NS	NS	UP	UP
Type 1 pneumocytes	NP	NP	NP	UP	NS	NP	NP
Type 2 pneumocytes	UP	UP	DOWN	DOWN	NS	DOWN	NP
Ciliated cells	UP	NP	NP	UP	UP	NS	NP
Goblet cells	NS	NP	NP	NS	NP	NP	NP
Club cells	DOWN	NP	NP	UP	UP	NS	UP
Smooth muscle cells	NS	NP	NP	DOWN	NS	NS	NP
Interstitial fibroblast	UP	NP	NP	NS	UP	UP	NS
Lipofibroblast	NS	NP	NP	DOWN	UP	UP	DOWN
Mesothelial cells	UP	NP	NP	DOWN	NS	NP	NP
Lung::Dcn stromal	NP	UP	UP	NP	NP	NP	NP
Lung::Gucy1a1 stromal	NP	DOWN	UP	NP	NP	NP	NP
Lung::Ihip stromal	NP	NS	UP	NP	NP	NP	NP
Lung::Npnt stromal	NP	NS	UP	NP	NP	NP	NP
Lung::leukocyte	NP	UP	DOWN	NP	NP	NP	NP
Lung::lung endothelial	NP	UP	UP	NP	NP	NP	NP
Lung::mast cell	NP	UP	NS	NP	NP	NP	NP
Lung::myeloid cell	NP	DOWN	UP	NP	NP	NP	NP

**Figure 3-Figure supplement 3. Comparison of the originally reported cell type-associated increase in transcriptional noise with the results obtained with Scallop.** The content of the first three columns was drawn from the original publications (*Angelidis et al.*; *Kimmel et al.*). More specifically, *Angelidis\_TN* is the transcriptional noise per cell identity on the Angelidis dataset (from their figure 2); *Kimmel\_OD* is the gene overdispersion per cell type on the Kimmel dataset (from their figure 2B); and *Kimmel\_DC* is the cell-cell heterogeneity per cell identity measured as the Euclidean distance to the centroid of the cell identity for a particular age. Columns 4-7 summarize the results of our analysis of age-related loss of cell type identity in the murine lung. Specifically, *Angelidis\_S*, *Kimmel\_S*, *TMS\_FACS\_S* and *TMS\_drop\_S* report the transcriptional noise per cell identity on the four datasets, measured as the difference in median membership score between young and old individuals. The cell identities used are those drawn from Angelidis. Since some cell identities from Kimmel dataset did not have a 1:1 correspondence to the Angelidis cell identities, they are shown using their original notation at the bottom of the table ("Additional cell identities"). UP/DOWN: age-related increase/decrease in noise, NS: the difference in noise between young and old individuals is not statistically significant. NP: the cell identity was not present in the dataset in sufficient amounts to perform the analysis. For most cell types, it can be concluded that there is little overlap between cell identity-specific noise measurements across datasets and methods

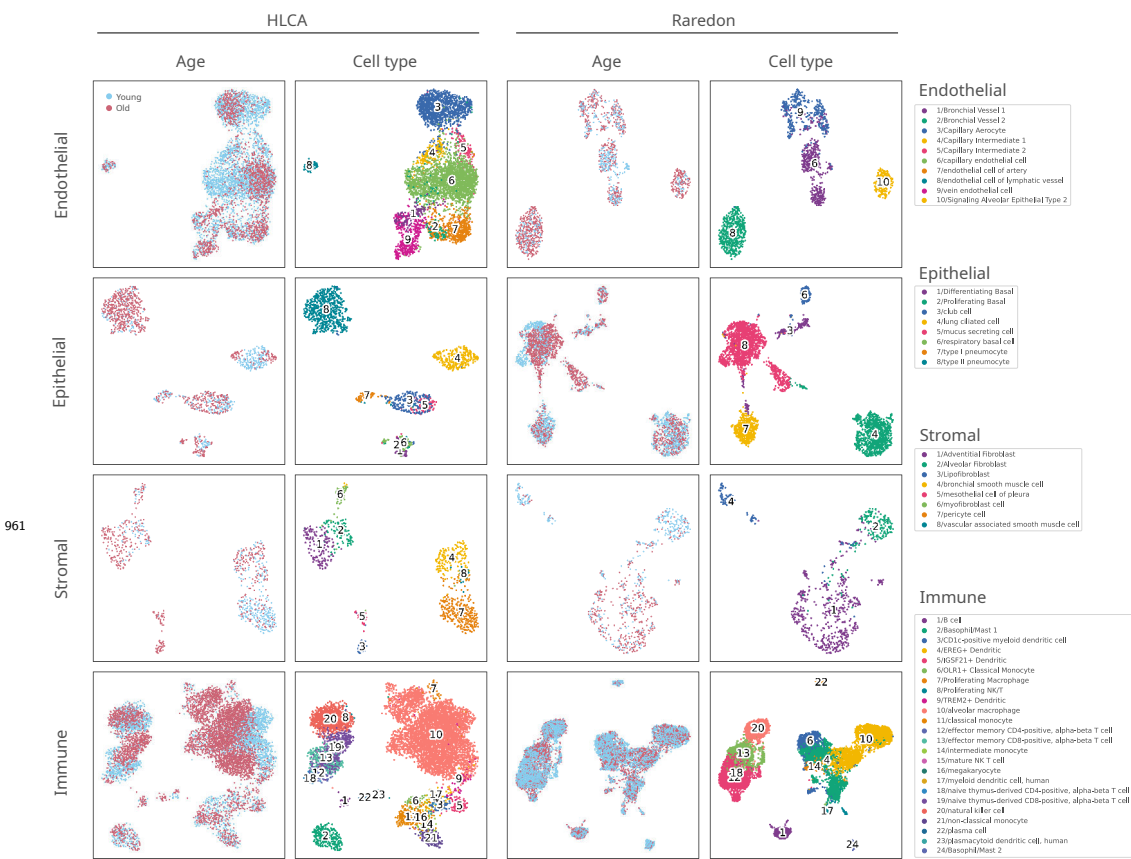


**Figure 4-Figure supplement 1. Composition of the two scRNAseq datasets of the human aging lung used in this figure.** The UMAP plots with the age and cell type identity annotations are shown for each tissue compartment (endothelial, epithelial, stromal and immune) and each dataset separately.

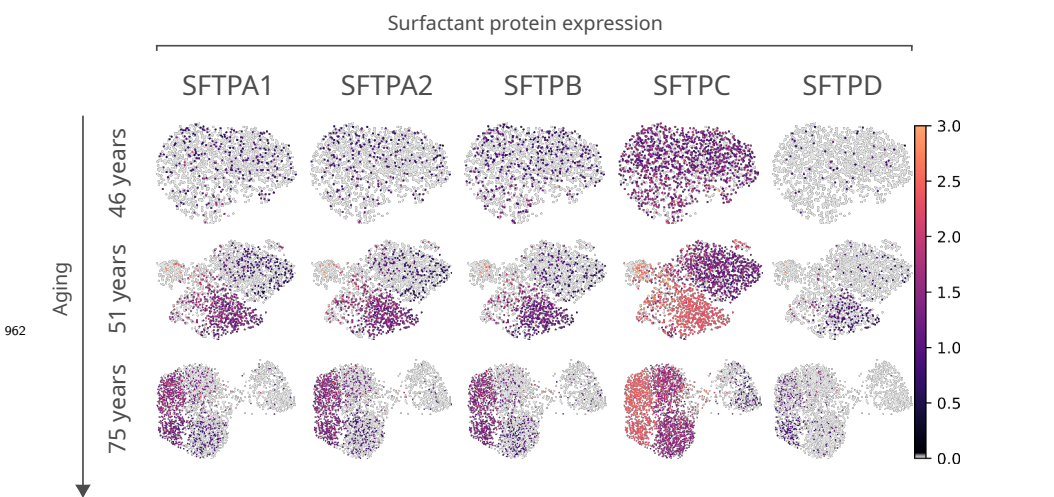


**Figure 5-Figure supplement 1. Expression of surfactant protein genes by human alveolar macrophages.** Differential expression by alveolar macrophage cell clusters of the genes coding for surfactant proteins *SFTPA1*, *SFTPA2*, *SFTPB*, *SFTPC*, and *SFTPD* is shown for three donors (aged 46, 51 and 75) of the *Travaglini et al.* (HLCA) dataset.